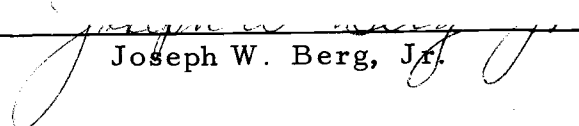AN ABSTRACT OF THE THESIS OF

Leland Timothy Long for the Doctor of Philosophy
      (Name)   (Degree)

in   Geophysics   presented on November 8, 1967
      (Major)   (Date)

Title: TRANSMISSION AND ATTENUATION OF THE PRIMARY

SEISMIC WAVE, Δ = 100 TO 600 KM

Redacted for Privacy

Abstract approved: _____
                               Joseph W. Berg, Jr.

The character of the primary seismic wave in the

range of distances between 100 and 600 km is affected by

such factors as the nature of the source, exponential

attenuation, crustal structure, type of wave propagation,

recording site geology and instrument response. The

first arrivals from the GNOME and SHOAL nuclear explo-

sions were analyzed to show the important effects of the

above factors. Crustal structures were developed to ex-

amine the type of wave propagation, geometrical attenua-

tion, and Q versus depth structure. Within the frequency

bands delineated by the instrument response, above 2 cps,

and the reliable source energies, exponential attenuation

and surface geology explained the major spectral varia-

tions in the first arrivals. Amplitude variations were

explained almost entirely by geometrical and exponential attenuation. Techniques for measuring exponential attenuation were developed and applied. The Q values obtained were primarily between 100 and 200.

TRANSMISSION AND ATTENUATION
OF THE PRIMARY SEISMIC WAVE,
Δ = 100 TO 600 KM

by

LELAND TIMOTHY LONG

A THESIS

submitted to

OREGON STATE UNIVERSITY

in partial fulfillment of

the requirements for the

degree of

DOCTOR OF PHILOSOPHY

June 1968

APPROVED:

Professor of Geophysics

In Charge of Major

Chairman, Department of Oceanography

Dean of Graduate School

Date thesis is presented November 8, 1967

Typed by Elaine R. Justice for   Leland Timothy Long

ACKNOWLEDGEMENTS

During my tenure as a graduate student I was the recipient of a National Aeronautics and Space Administration fellowship from September 1, 1965 to August 31, 1966. This honor was appreciated very much.

TABLE OF CONTENTS

LIST OF TABLES

LIST OF FIGURES

LIST OF APPENDIX FIGURES

TRANSMISSION AND ATTENUATION OF THE PRIMARY SEISMIC WAVE,

$\Delta = 100$ TO 600 KM

INTRODUCTION

Seismograms of primary seismic waves generated by

explosions provide important information about the effects

of transmission and attenuation along the propagation

paths of the waves. These effects are displayed as varia-

tions in waveform and traveltime, and at ranges of 100 to

600 km they are caused by the structural and material

properties in the crust and upper mantle. The object of

this research is to determine the effects of transmission

and attenuation responsible for molding the waveforms of

the first compressional arrivals from explosive sources.

The analysis will then be extended to delineate the

source information which is reliably transmitted through

the earth to the ranges of interest in this research.

The more important factors in determining the effects

of transmission and attenuation include: surface layer-

ing, absorption and scattering mechanisms, crustal struc-

ture, type of wave propagation, and noise or contamina-

tion. The waveform of the first arrival is influenced in

addition by source characteristics and instrument response. Each waveform, therefore, derives its character from some combination of the above factors in which the relative influence of any one factor depends on the arrival considered.

The specific effects of the factors influencing the waveform of the first arrival have been extensively analyzed individually. However, examinations of the first arrivals from 100 to 600 km from explosions have been limited, for the most part, to measurements of crustal structure, traveltime, amplitude, and amplitude attenuation. These measurements were obtained primarily from numerous seismic refraction lines which have been established in the western United States (Pakiser, 1963; Pakiser and Steinhart, 1964). Examinations of the first arrivals indicate, in particular, that the depth to the Moho varies regionally from 20 to 55 km. They also indicate that amplitudes in the range (r) of 100 to 600 km generally attenuate as r^{-3} (Romney, 1959; Romney et al, 1962), and that estimates of exponential attenuation in terms of a specific dissipation function, 1/Q, from amplitudes give Q values of 430 to 610 where head wave

geometrical spreading has been assumed (Ryall and Stuart, 1963). Ryall and Stuart also indicate that a Q of 200 is obtained for the crust from the $\overline{P}$ arrivals by assuming cylindrical spreading of the wavefronts.

Werth, Herbst, and Springer (1962) and Springer (1966) obtained a good agreement with observed arrivals by using assumed structure, material properties, and type of wave propagation to derive waveforms and amplitudes from source characteristics. However, a good comparison does not necessarily imply that the correct structural and material properties have been chosen. This technique was also applied by Laun (1965) to the reverse problem of predicting source characteristics from distant recordings. Laun pointed out, however, that the success of the technique depended on the proper choice of the type of wave propagation.

In this thesis the greatest emphasis is placed on exponential attenuation since it constitutes a major contribution to the molding of the wavform. Techniques are developed and utilized to measure attenuation directly from the waveform by using its diagnostic characteristic, exponential amplitude decay. On the other hand, factors

such as surface layering, type of wave propagation, and source character are neither as regular nor as prominent. Consequently, the relative importances of these factors are estimated by theoretically generating characteristic waveforms and comparing them to the observed waveforms.

The contents of this thesis are presented as follows in the subsequent chapters. The chapter entitled "Data" discusses the data used and pertinent information about the instrumentation. The analysis of the data for the effects of transmission and attenuation is discussed in the chapter entitled "Analysis". In the chapter entitled "Source Energy Transmission", the results of the analysis chapter are extended to delineate the source information reliably transmitted through the earth. Finally, the major conclusions resulting from this research are presented and discussed in the chapter entitled "Discussion and Conclusions".

DATA

The seismograms used in this research were recorded
by the U.S. Geological Survey's long-range seismic-
refraction equipment. Calibration of the recording sys-
tem was described by Warrick et al (1961). The frequency
response curves of the recording system, normalized am-
plitude and phase, are shown in Figures 1a and 1b, res-
pectively. They apply to the total recording system,
including seismometer, amplifiers, and magnetic tape, and
equate the ground particle velocity to record amplitude.
The response curves were derived from a consideration of
impulse, shake table, and electric shock tests. The in-
verse Fourier transform of the illustrated phase and am-
plitude response from 0.5 to 30 cps, which is the system's
velocity impulse response for those frequencies, is shown
in Figure 1c. Because the response is flat above two cps,
the record amplitude could be directly related to the
particle displacement[1] by

[1]Personal communication: John C. Roller, Geophysicist,
U.S. Department of Interior, Geological Survey, Branch of
Crustal Studies. Lakewood, Colorado. November 13, 1964.
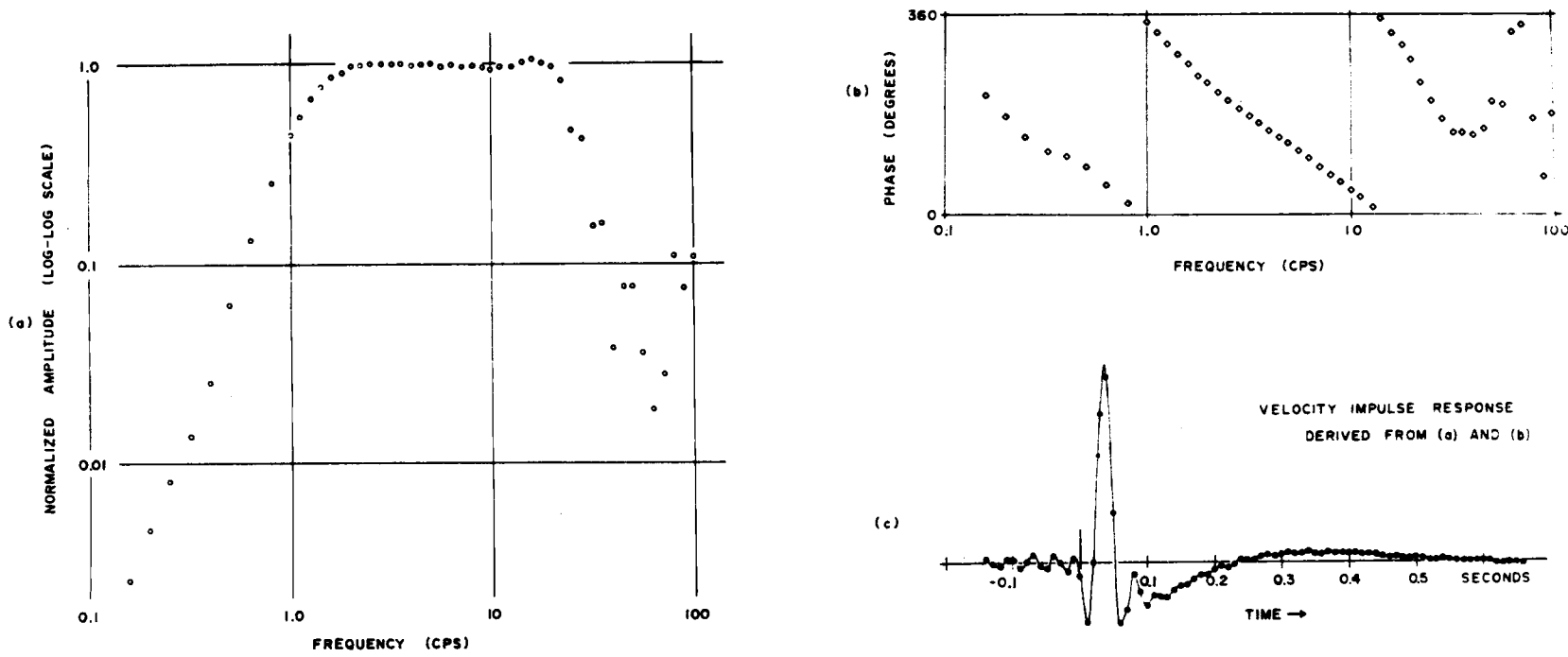
Figure 1. Total system response characteristics, ground particle velocity to record trace: (a) normalized amplitude response, (b) phase response, (c) velocity impulse response, inverse transform of amplitude (a) and phase (b). Data for (a) and (b) were furnished by U. S. Geological Survey.

$$D = \frac{5}{f} V \frac{S}{C} \tag{1}$$

where: D = particle displacement in millimicrons;

V = calibration voltage in microvolts (rms);

C = peak-to-trough amplitude of the calibration

trace;

S = trace amplitude, peak-to-trough; and

f = frequency in cycles per second.

Consequently, the particle velocity is given by

$$A = 10 \pi V \frac{S}{C} \tag{2}$$

where: A = particle velocity in millimicrons per second.

The seismograms investigated were from refraction

lines for the GNOME and SHOAL nuclear explosions. Table

I-a lists the relevant source information. The code

TABLE I-a. RELEVANT SOURCE INFORMATION.

Event	Date	Latitude Longitude	Yield Kt	Depth M	Medium
GNOME	Dec. 27,1962	N 32°15'49" W 103°51'57"	3.1$\pm$0.5	361	Salt
SHOAL	Oct. 26,1963	N 39°12'00" W 118°22'49"	12$\pm$2	367	Granite

TABLE I-b. RECORDING SITE DATA, <u>GNOME</u>.

Station Name	Traveltime sec	Range km	Latitude deg	min	Longitude deg	min
Mike	6.46	30.8	32°	33.17'	103°	49.02'
Golf	12.3	69.6	32	51.27	103	37.01
Papa	21.75	128.	33	23.84	103	39.80
Sierra	25.96	155.	33	37.84	103	38.77
Quebec	29.17	177.	33	49.92	103	34.72
Tango	32.32	193.	34	00.04	103	28.45
Lima	34.27	212.	34	07.79	103	31.49
India	38.76	238.	34	25.41	103	32.76
Hotel	45.30	297.	34	53.87	103	24.46
Kilo	51.84	355.	35	24.04	103	18.95
Juliet	62.08	430.	36	05.84	103	07.92

TABLE I-c. RECORDING SITE DATA, <u>SHOAL</u>.

Station Name	Traveltime sec	Range km	Latitude deg	min	Longitude deg	min
Papa	26.15	154.3	39°	18.23'	116°	35.75'
Tango	31.51	200.3	39	35.05	116	06.49
Sierra	36.75	238.7	39	31.92	115	38.60
Romeo	42.22	283.0				
Quebec	47.47	325.5	39	33.55	114	37.85
Kilo	57.79	409.8				
Juliet	63.87	455.2	39	39.98	113	07.59
India	69.90	500.3	39	40.70	112	35.95
Hotel	75.50	544.3				

names of the recording units, latitudes, longitudes, ranges, and traveltimes are given in Tables I-b and I-c. Each recording unit consisted of a linear array of four to six geophones (natural frequency of one cps, vertical component) placed in line with the shot and separated by approximately 0.5 km. The arrivals were recorded on both film and magnetic tape.

Figure 2 shows the locations of the explosions and recording stations. The GNOME refraction line is in the eastern portion of New Mexico on the western edge of the Great Plains. The SHOAL refraction line is in the Basin and Range Province of Nevada and Utah. The applicability of the results presented in this thesis is thus limited to these regions.

One trace from each station along the GNOME line was digitized, where possible, at an interval of 0.004 sec using a traveling microscope. The traces at stations Mike and Golf were not digitized because they were at ranges less than the minimum considered applicable in the analysis. The recording at station Hotel lacked sufficient amplitude for digitization and the recording at station Juliet was severely contaminated with noise and was not used. The traces that were digitized for GNOME are shown in Figure 3
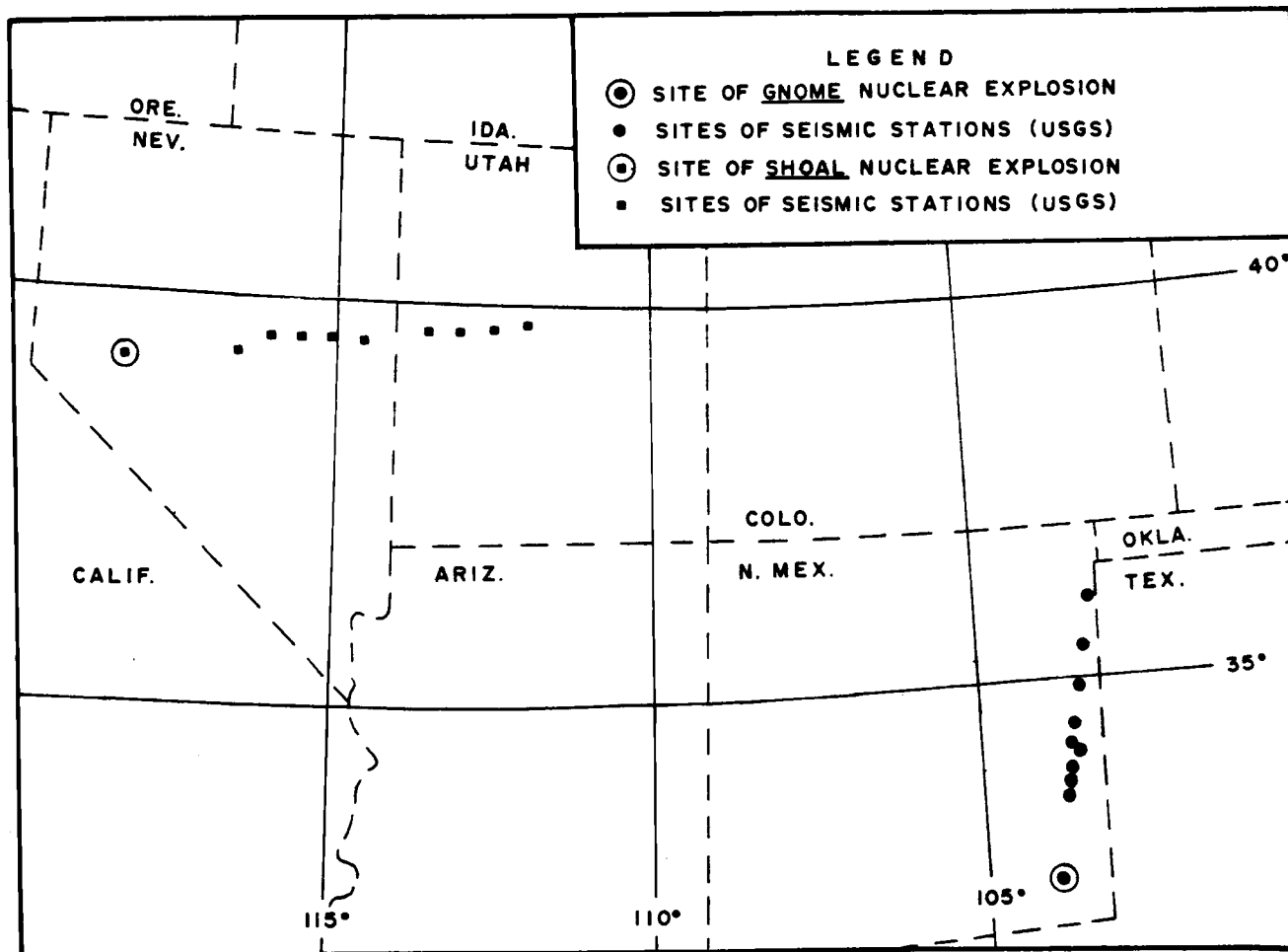
Figure 2. Location of shot sites and recording stations.

GNOME

SHOAL

PAPA
128

0.5 SEC

SIERRA
155

QUEBEC
177

TANGO
193

LIMA
212

INDIA
238

HOTEL
297   NOT DIGITIZED

KILO
355

JULIET   NOT DIGITIZED
435   0.5 SEC.

PAPA
154   I SEC.

TANGO
200

SIERRA   NOT DIGITIZED
238

ROMEO
282

QUEBEC
325

KILO
409

JULIET
455

INDIA
500

HOTEL
544   I SEC.

——— TRACES THAT WERE DIGITIZED

------ DIGITIZED TRACES CORRECTED FOR NON-ZERO NET AREA
AND INTERFERING ARRIVALS WHERE POSSIBLE

▼ TERMINATION POINTS FOR FIRST ARRIVAL

Figure 3. Seismic traces used in this research.

as the solid lines. Since a zero net particle displace-
ment requires that the particle velocity traces have zero
net area beneath the curves, all digitized traces of GNOME
except Papa were adjusted to a zero net area. For sta-
tions Sierra, India, and Kilo the adjustment included re-
moving the effect of a secondary arrival. The corrected
arrivals are shown in Figure 3 as the dotted lines where
they differed from the uncorrected arrivals. The dura-
tions of the corrected first arrivals used in the analysis
are indicated by the arrows and were determined from a com-
parison of theoretical and observed pulses.

The first three to five seconds of all the SHOAL
traces except those at station Sierra were digitized
directly from the magnetic tapes at an interval of 0.01
sec. No magnetic tape was available for station Sierra.
The digitized traces were calibrated by comparison to the
calibrated analog traces. The arrivals in the array at
each station for SHOAL were stacked to reduce the noise
level and determine the average waveform. Delay times
for stacking were unambiguously determined to within ± 0.02
sec by comparing the first half-cycles of the arrivals in
each array. The amplitudes for any given array were not
normalized to uniform magnification for the purpose of

stacking because the variation in the calibration ampli-

tude was not sufficient, in comparison to the variation

in signal amplitude, to warrant corrections. The stacked

SHOAL arrivals are shown in Figure 3. The length of the

first arrival considered in the analysis is indicated by

the arrow and was determined from a comparison of theoret-

ical and observed pulses. The seismograms in Figure 3

constituted the principal data for this thesis.

ANALYSIS

The operator theory and the Fourier transform used to
analyze the effects of transmission and attenuation are
discussed in the first section of this chapter. Since the
most important factors in transmission and attenuation are
source characteristics, surface layering, exponential at-
tenuation, and type of wave propagation, each of these ef-
fects is considered separately in succeeding sections of
this chapter. The section on source characteristics dis-
cusses some important limitations imposed by the source
character, and in particular some limitations on the fre-
quencies of energy available for seismic wave propagation.
The section on surface layering describes how an initial
pulse can be contaminated by multiple reflections within
the surface layers. Similar effects, however, may be pro-
duced by waves traveling by different paths. The indepen-
dently determined crustal velocity structures are present-
ed in a section preceding the sections on exponential at-
tenuation and type of wave propagation since these latter
sections require some knowledge of the velocity structure.
Then, in the section of the theory of exponential attenu-
ation, the combined effects of all forms of seismic

energy absorption and scattering is developed and tech-
niques are applied to find Q values and a Q versus depth
profile. The final section of this chapter describes the
effects of various types of wave propagation with particu-
lar emphasis on distinguishing between head and direct
waves. The factors responsible for molding the waveform
are treated individually in the various sections of this
chapter. The effects these factors generate and the am-
biguities among the effects are also discussed but not all
to the same extent.

Operator theory

Operator theory is used extensively in the analysis
of the waveforms and to generate theoretically the effects
of transmission and attenuation. The operator represents
a mathematical equivalent for transmission and attenuation
mechanisms in that it transforms an initial or source
waveform into its final or observed form. In the applica-
tion of operator theory to the analysis, the operator is
assumed to be linear, passive, stable, time invariant and
causal. Linearity requires that an operator affect all
initial waveforms in the same manner regardless of ampli-
tude or character. The passivity condition requires that

the observed waveform be derived entirely from the initial waveform and is violated by microseismic noise. The conditions of stability and time invariance are not easily violated in the earth. Causality is required by all physically realizable operators since the character of an observed waveform cannot depend on future events. Consequently, causal operators in the time domain are zero for negative time.

Fourier integral transform theory is used in the analysis to develop the mathematical operator. In the frequency domain, the relation between the Fourier transform or, equivalently, the spectrum of the initial waveform, $A_o(w)$, and the spectrum of the final waveform, $A(w)$, is expressed in operator notation as $A(w) = 0_p(w)A_o(w)$. The implied operation is multiplication. In the time domain the relation between the initial waveform, $A_o(t)$, and the final waveform, $A(t)$, is expressed as $A(t) = 0_p(t)*A_o(t)$. The operator, $0_p(w)$, in the frequency, w, domain is the Fourier transform of the operator, $0_p(t)$, in the time domain. The operation implied by (*) is convolution and, for a continuous function convolved with a causal operator, is defined as

$$A(t) = 0_p(t) * A_o(t) = \int_{-\infty}^{t} 0_p(t-t') A_o(t') \, dt'. \tag{3}$$

For finite data digitized at an interval of Δt, convolution is defined as

$$A(t_k) = \sum_{j=1}^{N} 0_p(t_k-t_j) A_o(t_j) \Delta t \tag{4}$$

where: N = number of evenly spaced samples of the

seismic trace; and

$$0_p(t_k-t_j) = 0_p \left[(t_k-t_j) \pm N\Delta t \right].$$

The summation need only be computed up to j equal to k when both 0_p and A_o are causal and the significant portion of their energy is concentrated in the first half of the digitized time period.

The Fourier transform pair for continuous data of infinite length is defined by

$$g(w) = \frac{1}{2\pi} \int_{-\infty}^{\infty} f(t) \exp(-iwt) \, dt$$

$$\tag{5}$$

$$f(t) = \int_{-\infty}^{\infty} g(w) \exp(+iwt) \, dw$$

where: $f(t)$ = seismic trace in the time domain;

$g(w)$ = spectrum in the frequency domain; and

$i = \sqrt{-1}.$

For digital seismic data, the Fourier transforms reduce to finite summations over the frequencies, w_j, and times, t_k, (Huang, 1966) as follows:

$$g(w_j) = X_j + iY_j = G_j \exp(i\phi_j)$$

$$f(t_k) = \Delta w \sum_{j=1}^{N} G_j \cos(2\pi kj/N + \phi_j) \qquad (6)$$

$$= \Delta w G_N + 2\Delta w \sum_{j=1}^{N/2} G_j \cos(2\pi kj/N + \phi_j) - \Delta w G_{N/2}$$

where: $G_j = (X_j^2 + Y_j^2)^{\frac{1}{2}}$ = the modulus;

$\phi_j = \text{Tan}^{-1}(Y_j/X_j)$ = the phase angle;

$X_j = \dfrac{1}{N\Delta w} \displaystyle\sum_{k=1}^{N} f(t_k) \cos(2\pi kj/N);$

$Y_j = \dfrac{1}{N\Delta w} \displaystyle\sum_{k=1}^{N} f(t_k) \sin(2\pi kj/N);$ and

N = number of evenly spaced samples of the seismic trace.

In the time domain, the digitization specifies only N independent values, and thus only N independent values can exist in the frequency domain. These are the N/2 real and N/2 imaginary numbers in the spectrum, or the N/2

values of the modulus and phase in equations (6). The
highest independent frequency, the folding frequency, is
50 cps for the SHOAL traces digitized at 0.01 sec inter-
vals and 125 cps for the GNOME traces digitized at 0.004
sec intervals. Since the instrument response limits the
observable frequencies to below 30 cps, the digitizing in-
tervals that were used are entirely adequate.

Source characteristics

The source represents the initial condition to the
problem of transmission and attenuation and, as such,
imposes certain important limitations. The most important
limitations concern the spectral distribution of energy
and the complexity of the initial waveform. However, be-
fore the extent of these limitations can be determined,
the portion of the source responsible for the character
of the arrivals from 100 to 600 km must be isolated.
This isolation involves a number of difficulties.

For both GNOME and SHOAL, recordings of the radial
particle velocity in the horizontal plane of the explo-
sion at ranges of 0.585 and 0.298 km, respectively (ob-
tained from the Sandia Corporation through the courtesy

of William Perret and Wendell Weart), are shown in Figure

4a. Secondary arrivals in both GNOME and SHOAL can add to

the source considerable character which does not contrib-

ute to the distant arrivals. For example, the arrival at

0.06 sec in SHOAL, Figure 4a, may represent a P to SV con-

version. Other secondary arrivals in both GNOME and

SHOAL are not as distinct. Although the P to P surface

reflection has a relatively small amplitude in a radial

direction of the horizontal plane, it could contribute

considerably to distant arrivals which were radiated

away from the source at an angle of about 35° from the

vertical.

In the frequency domain, a secondary arrival causes

the modulus of a spectrum to be modulated by

$$\left[A^2 + B^2 + 2AB\cos(wT) \right]^{\frac{1}{2}} \tag{7}$$

where: A = amplitude of first arrival;

B = amplitude of secondary arrival; and

T = time delay.

When the amplitudes are comparable, the resulting spec-

trum can deviate considerably from the spectrum of a

single arrival. The minima in the SHOAL spectrum (see
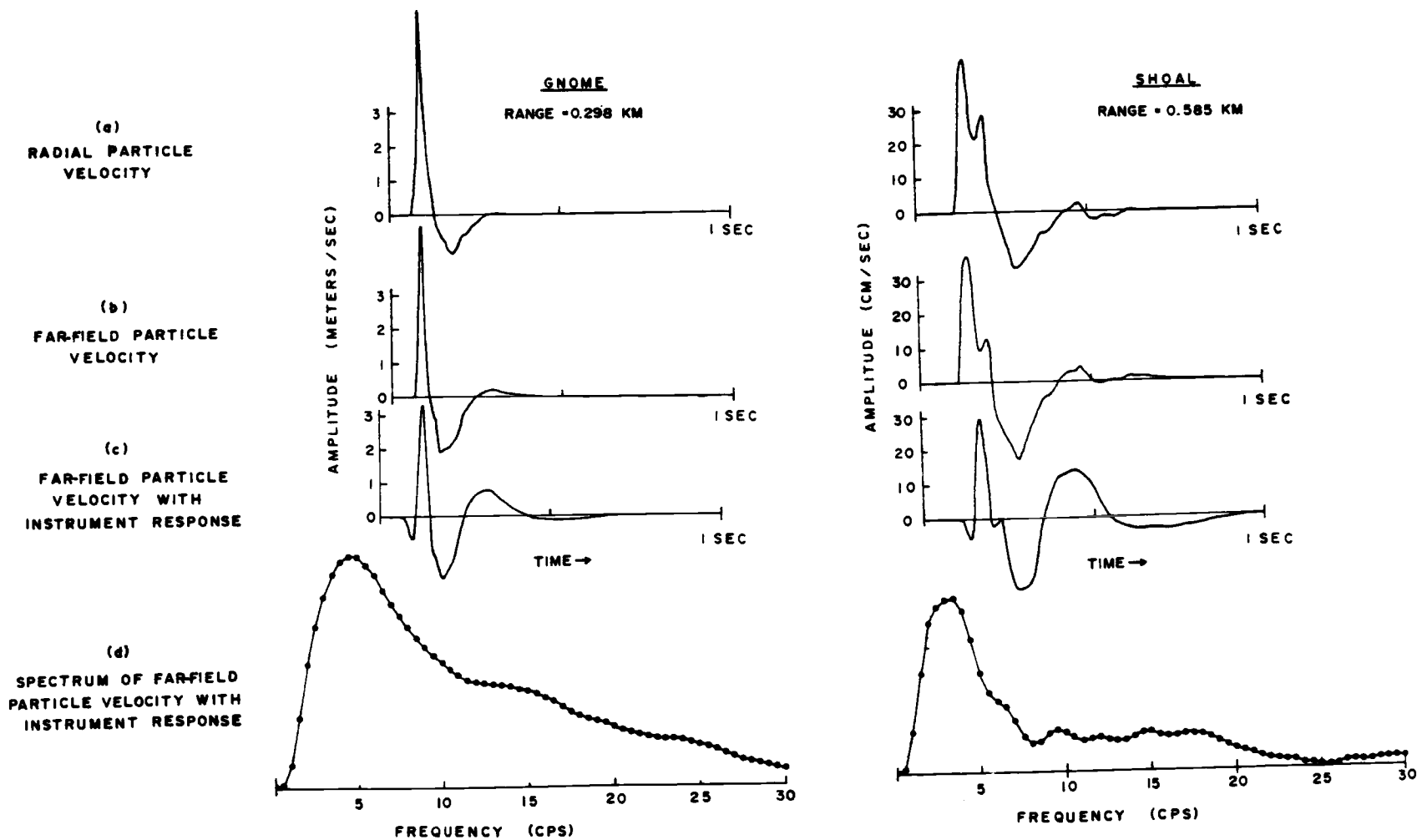
Figure 4. Source data: (a) radial particle velocity, (b) far-field particle velocity, (c) far-field particle velocity with instrument response, (d) spectrum.

Figure 4d) at 8 and 25 cps are consequences of the second-
ary arrival at 0.06 sec. The P-wave surface reflection
could, as can be seen by inserting a -B for B in equation
(7), reduce the energy available in the lower frequencies
for recordings at distance. Fuchs (1966) in solving for
the P-wave transfer function of a point source in a layer-
ed medium also observed that sources near the surface re-
jected the low frequencies strongly and that the low-fre-
quency rejection band broadens as the source approaches
the surface. Consequently, uncertainties in the inter-
fering arrivals caused by possible surface reflections
will strongly restrict any direct comparison of the
sources with distant arrivals.

Nevertheless, when secondary arrivals do not inter-
fere significantly, some measure of the limitations im-
posed by the initial conditions due to the source can be
gained since the portion responsible for the character of
the arrivals at large ranges can be derived from the ob-
served particle velocity. An expression for particle
velocity can be derived from a displacement potential
function which is a solution to the scalar wave equation
for a symmetrical source in a homogeneous, isotropic, and
elastic medium. By differentiating with respect to time

and range, the resulting expression for particle velocity is

$$v(\tau) = - \frac{\partial}{\partial r} \frac{\partial}{\partial t} \left[\phi(\tau)/r \right]$$

$$= \phi''(\tau)/rc + \phi'(\tau)/r^2 \qquad (8)$$

where: $v(\tau)$ = particle velocity;

$\phi(\tau)/r$ = displacement potential;

τ = t-r/c = reduced time; and

c = compressional wave velocity.

Since for large r the term $\phi'(\tau)/r^2$ is negligible, the term $\phi''(\tau)/rc$ is essentially responsible for the character of the distant arrival. The solution of the differential equation, equation (8), for $\phi''(\tau)/rc$ is given in digital form as

$$\phi''(\tau_i)/rc = v(\tau_i) - \frac{c}{r} \sum_{j=1}^{i} v(\tau_j) \exp\left[\frac{c}{r}(\tau_j - \tau_i)\right] \Delta\tau \qquad (9)$$

The derived far-field particle velocities, $\phi''(\tau)/rc$, for GNOME and SHOAL are shown in Figure 4b. The derived far-field particle velocities with the instrument response and their spectra are shown in Figures 4c and 4d, respectively. At 0.298 and 0.585 km the effect of the near-field com-

ponent, $\phi'(\tau)/r^2$, is small but noticeable.

The far-field character is not complex and closely resembles the expected response of a spherical cavity to an impulsive source, (Berg, Trembly, and Laun, 1964; Trembly and Berg, 1966). The spectra for different sources, however, show important differences in frequency content. GNOME shows significant energy from two cps up to and above ten cps while SHOAL shows significant energy from 1.5 cps to five cps only. The disparity in frequency content near the source is caused largely by the different yields (Berg and Papageorge, 1964 - see Table I-a). The differences in media, salt for GNOME and granite for SHOAL, and in the ranges at which measurements were made undoubtedly contribute to the disparity in frequency content also. The implication of the spectral distribution of energy is that the analysis for SHOAL must be limited to frequencies between 1.5 and five cps while the analysis for GNOME can be extended from two cps up to at least ten cps. Because of this, no reliable source-related information can be obtained for frequencies outside these limits.

Surface layering effects

The near surface geological structure can vary considerably in velocity, thickness, and density, and can significantly alter the character of the first arrivals, particularly for frequencies above two cps. An unconsolidated alluvial surface layer can extend to depths greater than 0.7 km and above the water table its velocity can be as low or lower than two km/sec. The underlying rocks can either increase gradually to about six km/sec or show a six km/sec velocity close to the boundary. Near-surface velocity structure, if known, could help understand or make it possible to remove theoretically the surface layering effects on an incident pulse. Such information was not available at the recording locations, but possible effects were considered theoretically.

To illustrate the effect of a surface layer, an extreme case of a two km/sec, two gm/cm^3 layer overlying a six km/sec, 2.5 gm/cm^3 basement was calculated. The theoretical technique for calculating the general case and the calculation for a single layer is presented in Appendix I. In essence the distortion of a pulse at normal incidence is caused by multiple reflections

within the surface layer. The resulting surface motion

consists of a series of attenuated and delayed pulses al-

ternating in sign. In the Fourier frequency domain the

equivalent effect is expressed by the operator equation

(see Appendix I):

$$V_s(w) = \frac{4\alpha_2\rho_2 \exp\left[+iwh(1/\alpha_1 - 1/\alpha_2)\right] V_i(w)}{(\alpha_1\rho_1 + \alpha_2\rho_2)\left[1 + R\exp(+iw2h/\alpha_1)\right]} \tag{10}$$

where: $V_s(w)$ = spectrum at the surface;

$V_i(w)$ = incident spectrum;

α_k = compressional velocity in kth layer;

ρ_k = density in kth layer;

h = thickness of surface layer; and

$R = (\alpha_2\rho_2 - \alpha_1\rho_1)/(\alpha_2\rho_2 + \alpha_1\rho_1)$

= Rayleigh reflection coefficient.

The modulus of the operator is

$$4\alpha_2\rho_2\left\{(\alpha_2\rho_2 + \alpha_1\rho_1)\left[R^2 + 1 + 2R\cos(2wh/\alpha_1)\right]^{\frac{1}{2}}\right\}^{-1}. \tag{11}$$

Figure 5 shows the effect of this operator for thicknesses

of 0, 50, 100, 150, and 250 meters. These values span the

range of likely thicknesses of an unconsolidated alluvial

surface layer over a high velocity basement rock. The

FREE SURFACE

h = THICKNESS
OF SURFACE
LAYER

ρ_1 = 2.0 GM/CC

α_1 = 2 KM/SEC

ρ_2 = 2.5 GM/CC α_2 = 6 KM/SEC

	h METERS	APPARENT FREQUENCY
INCIDENT PULSE (QUEBEC 325 KM)	0	3.7
PARTICLE MOTION AT SURFACE	50	4.2
	100	4.3
	150	3.3
	250	---

TIME →
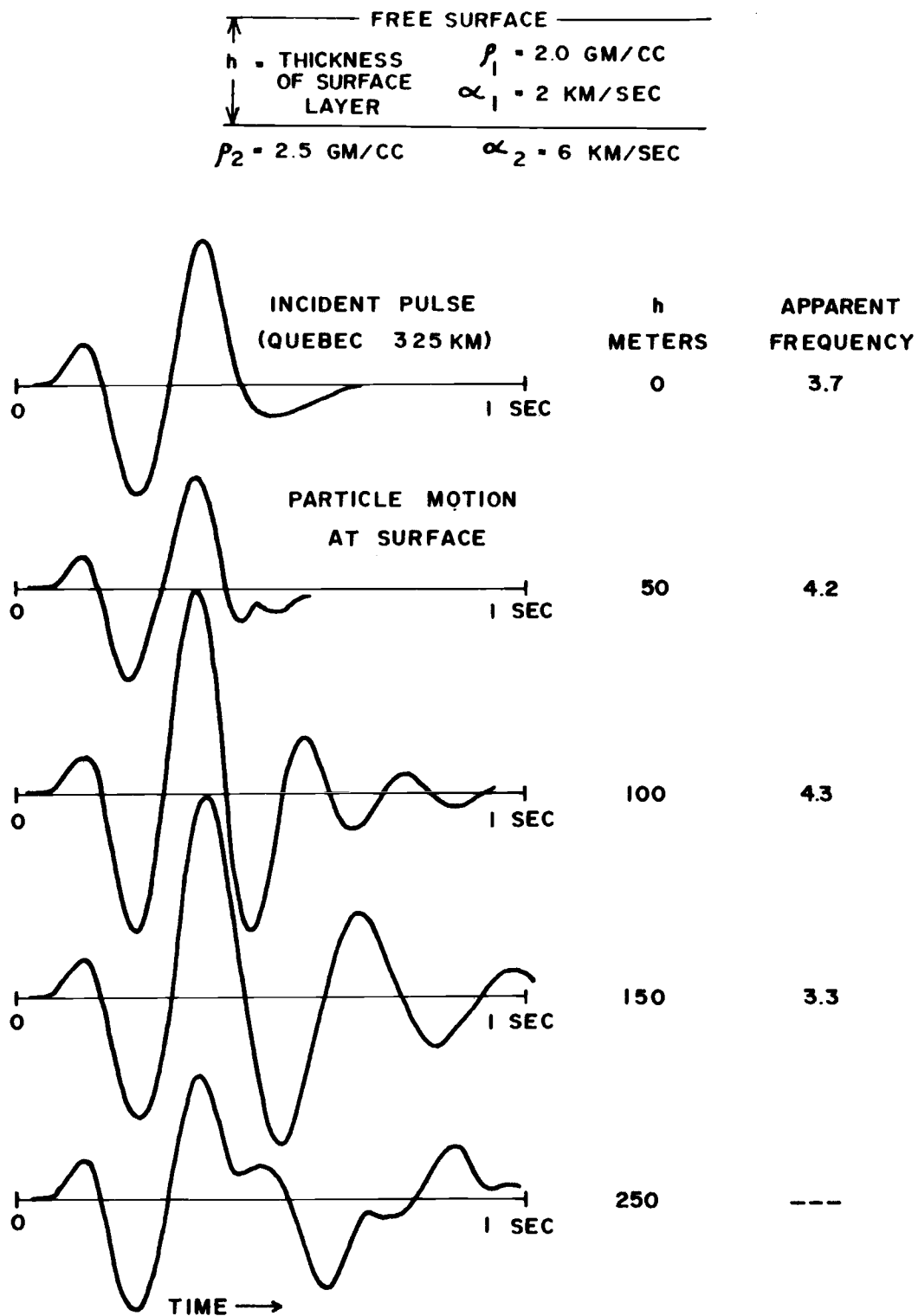
Figure 5.   Effects of four thicknesses (h) of surface
layering on a normal incident pulse.

arrival at station Quebec, SHOAL, was used for the incident pulse. As Figure 5 shows, the surface layer can strongly affect the amplitude, apparent frequency, and the duration of the arrival. The first cycle, however, was the least affected. The amplitudes in Figure 5 varied $\pm$ 25 percent and the apparent frequencies varied ± 0.5 cps. The duration of the arrival increased, as expected, with the thickness of the surface layer. Surface layers thicker than 600 meters would be required to separate the pulses.

Some of the theoretical waveforms illustrated in Figure 5 are similar to waveforms along the GNOME and SHOAL refraction lines. However, without measured velocity structures at each station, no conclusions can be drawn from these comparisons since secondary arrivals unrelated to surface layering may produce similar effects. In addition, lateral variations in velocity or thickness of the surface layer could cause a focusing of the incident wave and increase the variability of the amplitudes and waveforms. Nevertheless, the two most likely examples of the surface layer effect are stations Papa and Romeo along the SHOAL line. They compare favorably to theoretical arrivals for layer thicknesses of 250 and

100 meters, respectively.

The SHOAL line is in the Basin and Range Province, see Figure 2, where large thicknesses of unconsolidated alluvium over hard rock is a common geological occurrence. GNOME, on the other hand, is along the western edge of the Great Plains where the velocity structures usually consist of many layers with smaller contrasts. An increased number of layers with decreased contrasts reduces the effect of surface layers considerably, and perhaps, this accounts for the more uniform character of the GNOME traces.

The arrivals at stations Tango, SHOAL, and India, SHOAL, Figure 3, show a nine cps rider of considerable amplitude. The possibility that this is caused by a single surface layer was also examined. Although a single layer does predict spectral peaks at ten cps for thicknesses of 50, 150, and 250 meters, these peaks, even in this extreme case, are not sufficient to explain the high amplitude of the nine cps rider. More complicated velocity structures would need to be hypothesized to explain this observation. Surface materials do not always conform to the assumptions of elastic theory and are notorious distorters of high-frequency signals which,

perhaps, explains part of the present poor understanding of high-frequency seismic noise. The ultimate explanation of the high-frequency rider may involve signal generated noise, selected frequency amplification, or some other non-linear process.

Crustal structures

In this section the basic crustal structures for the GNOME and SHOAL refraction lines are presented. They do not differ significantly from the GNOME profile given by Stewart and Pakiser (1962) or the crustal structure given by Eaton (1963) near the SHOAL line. The development of the crustal structures was based essentially on travel-time curves and is presented in detail in Appendices II and III. In the waveform analysis, the structures are necessary to predict amplitudes and possible types of wave propagation. Variations in the attenuation parameters along the refraction lines must also be considered relative to the observed structure. Conversely, the waveform analysis leads to further refinements in the basic crustal structures.

The crustal structures for the GNOME and SHOAL refraction lines were developed individually since different

techniques were applied in the two analyses. The lateral

structural variations along the GNOME refraction line

were assumed to be entirely correctable. Consequently,

the structure was derived directly from the observed

traveltime data. The continuous velocity versus depth

profile shown in Figure 6a applies to the major portion of

the GNOME line. The most important features are the vel-

ocity gradients above and below the Moho and the depth of

54 km to the Moho.

Significant lateral variation in the structure did

occur along the SHOAL refraction line. Consequently,

models were generated until one was found that satisfied

the observed traveltime data. The generalized velocity

versus depth profile and the crustal model are shown in

Figures 6b and 6c, respectively. The most important

features are again the velocity gradients and the depths

to the Moho. If the velocity versus depth profile below

the Moho remains laterally constant, then the velocity

gradient determines the velocity at the Moho since the

depth to the Moho varied. The GNOME and SHOAL velocity

profiles are remarkably similar above 30 km and below

54 km in spite of the differences in location. In neither

case was the structure determined below 65 km. This
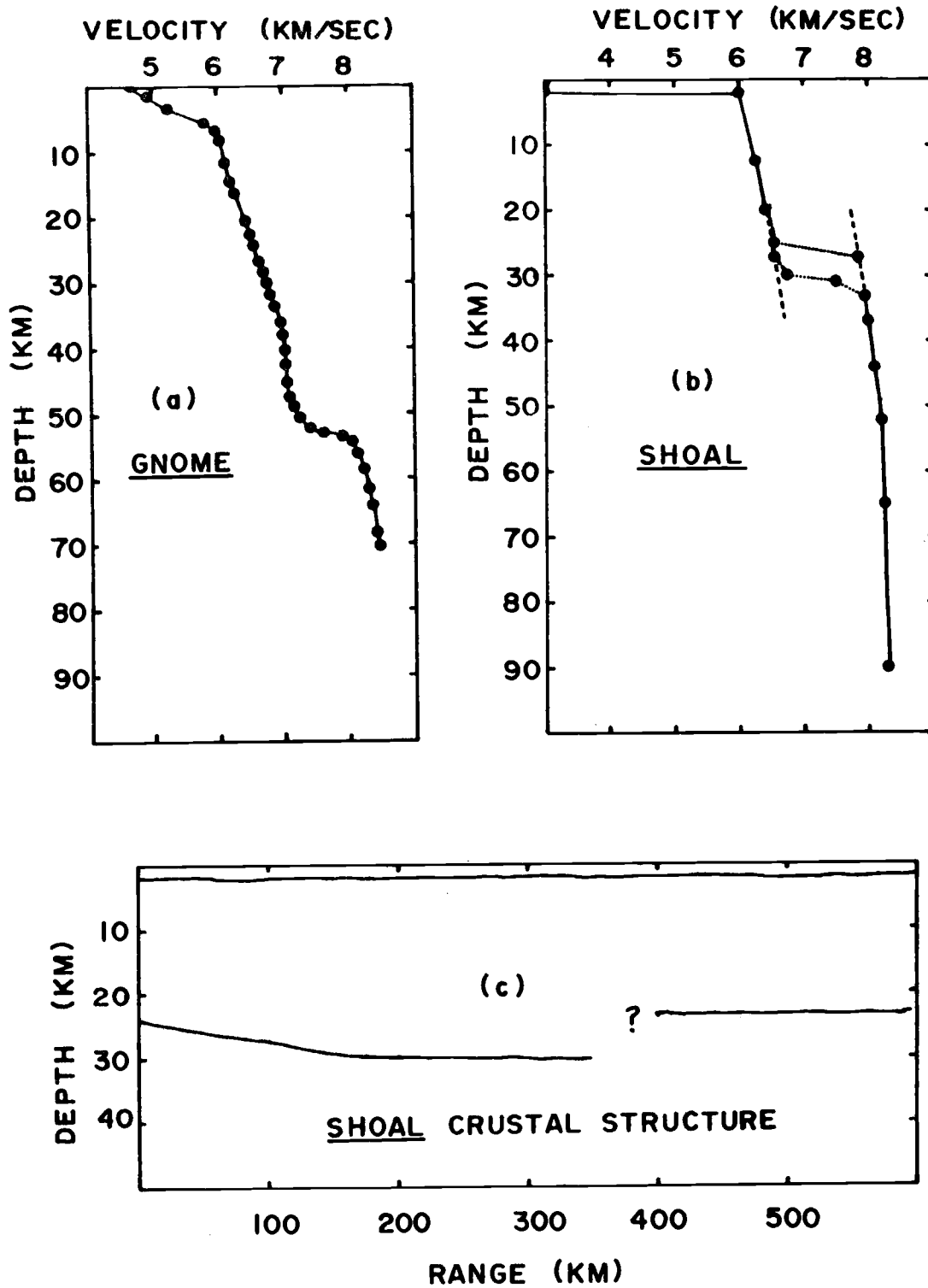
Figure 6.   Crustal structures: (a) GNOME velocity versus
depth profile, (b) SHOAL velocity versus depth
profile, (c) SHOAL crustal structure.

depth corresponds to the maximum depth of penetration for a direct wave.

Exponential attenuation

The investigations and measurements of both linear and non-linear loss mechanisms in the materials of the earth have been summarized by Howell (1963) and Knopoff (1964). These summaries indicate no general agreement as to the best explanation for seismic wave attenuation. However, the energy loss factor generally observed in laboratory and field measurements (White, 1965, p 107) is

$$\exp(-wt/Q). \tag{12}$$

In the observed form, equation (12), $1/Q$ is a frequency independent loss parameter or specific dissipation constant. In general, however, Q may be a function of frequency and medium.

In order to explain how Q is measured and the significance of these measurements, the analysis of exponential attenuation is divided into the following five parts: (A) a linear theory of attenuation is developed for a generalized Q; (B) a technique is developed and used to measure attenuation from spectral variations only;

(c) least-square values of Q are presented; (D) the implications of the combined spectral attenuation and amplitude measurements are considered; and (E) an attempt is made to determine attenuation as a function of depth.

A) <u>Theory</u>. - An absorptive or scattering medium can be characterized by complex elastic coefficients if, during each stress cycle, the loss of energy is a linear function of the maximum energy stored (White, 1965). The exact loss mechanism need not be specified in order to develop a loss factor for any type of linear wave propagation in terms of complex coefficients. The complex form of Lame's coefficients, λ_c and μ_c, may be expressed as

$$\lambda_c = \lambda + i\text{Sgn}(w)\lambda^*, \text{ and}$$
$$\mu_c = \mu + i\text{Sgn}(w)\mu^*.$$

(13)

The factor Sgn(w) is required to satisfy the equation $g(w) = \overline{g(-w)}$ relating the spectrum of a real function, $g(w)$, to its complex conjugate for negative w, $\overline{g(-w)}$.

For plane compressional waves the wave equation is written in spectral form as

$$(M + i\,\text{Sgn}(w)M^*)\frac{\partial^2}{\partial r^2} A(w,r) = -\rho w^2 A(w,r) \qquad (14)$$

where: $M = \lambda + 2\mu;$ and

$M^* = \lambda^* + 2\mu^*.$

A solution written as

$$A(w,r) = A(w)\,\exp(Wr) \qquad (15)$$

will satisfy the wave equation when

$$W = \pm\, iw(\rho)^{\frac{1}{2}}\left[M + i\,\text{Sgn}(w)M^*\right]^{-\frac{1}{2}}$$

$$= \pm\, iw(\rho/M)^{\frac{1}{2}}\left[1 - i\,\text{Sgn}(w)\frac{M^*}{2M} + \ldots\right] \qquad (16)$$

$$= \pm\, iw(\rho/M)^{\frac{1}{2}} \pm |w|\frac{M^*}{2M}(\rho/M)^{\frac{1}{2}}, \quad M^* \ll M$$

$$= \pm\, iw/V_p \pm \frac{|w|M^*}{2MV_p}, \quad (\rho/M)^{\frac{1}{2}} = 1/V_p.$$

Consequently, an approximate solution to the wave equation for a wave propagating in the direction of increasing range, r, is expressed as

$$A(w,r) = A(w)\exp\left[-iwr/V_p - |w|\,r/(2QV_p)\right] \qquad (17)$$

where: $1/Q = M^*/M.$

Also, Q and V_p may be functions of frequency.

When V_p and Q are constants with respect to frequency, equation (17) corresponds to the observed form, (see equation (12)). However, with frequency independent V_p and Q, equation (17) cannot satisfy the concept of causality. The concept of causality requires that a finite time, proportional to the distance, must elapse before a pulse arrives at a point distant from its source. When this applies, the existence of attenuation is a necessary and sufficient condition for dispersion. Furthermore, the Kramer-Kronig relation can be used to derive the dispersive or imaginary part of W from the attenuation or the real part of W. Futterman (1962) has derived and used the appropriate form of the Kramer-Kronig relation to generate the imaginary component of W from a real component expressed as

$$\text{Re}(W) = \frac{|w|}{2QV_p} = \frac{|w|}{2cQ'}\left[1 - \exp(-|w|/w_o)\right] \qquad (18)$$

where: c = non-dispersive phase velocity;

Q' = constant with respect to frequency; and

w_o = low-frequency cutoff.

The resulting high-frequency solution to the wave equation as given by Futterman (1962) is

$$A(w,r) = A(w) \exp \left\{ - \frac{|w| r}{2cQ'} \left[1 - \exp(-|w|/w_o) \right] + i\phi \right\} \quad (19)$$

where: $\phi = wr/V_p$;

$$V_p = c \left\{ 1 - \frac{1}{\pi Q'} \left[\text{Log}_e (\gamma |w|/w_o) \right] \right\}^{-1}; \text{ and}$$

$$\text{Log}_e (\gamma) = 0.5772157 = \text{Euler constant.}$$

As long as w_o is chosen significantly lower than the lowest frequency considered, equation (19) will very closely approximate the observed exponential attenuation with a constant Q as given by equation (12).

For reduced time, the non-dispersive, $V_p=c$, approximation to equation (17) with Q remaining a function of frequency is expressed for positive frequencies as

$$A(w,r) \cong A(w) \exp \left[-wr/(2cQ) \right] . \quad (20)$$

For purposes of analysis, equation (20) was generalized further by introducing a frequency-independent geometrical spreading factor, $f(r)$. Then, since the velocity and Q can also be functions of the medium, the exponent must be written as an integral along the propagation path, s, to

the range r:

$$\frac{w}{2} \int \frac{ds}{cQ} = \frac{w}{2} K(w,r).$$ (21)

The integral in equation (21) defines the function $K(w,r)$ which is also a function of frequency, w, and propagation path to the range r. The function $K(w,r)$ represents a direct index of the accumulated attenuation exhibited by an arrival. Consequently, the effective Q, $Q_{eff}(w,r)$, which may also be a function of range and frequency, is defined by

$$t/Q_{eff} = K(w,r)$$ (22)

where t is the traveltime to the range r, and Q_{eff} represents the average or bulk Q for a particular propagation path. Hence, the resulting generalized form of equation (20) used in the analysis of attenuation is

$$A(w,r) = A(w) f(r) \exp\left[\frac{-wt}{2Q_{eff}(w,r)}\right].$$ (23)

Where dispersion was of interest, the expression given by Futterman, equation (19), was used.

B) <u>Measurement of Q$_{ap}$</u>. - The initial spectrum, A(w),
and the geometrical amplitude term, f(r), applicable to
equation (23) represent unknowns which may be difficult to
determine reliably from measurements near the source and
which, consequently, should be eliminated. The initial
spectrum was eliminated by subtracting the natural loga-
rithms of equation (23) for two distinct ranges, r$_i$ and
r$_j$. In the resulting equation,

$$\text{Log}_e\left[A(w,r_i)/A(w,r_j)\right] = \text{Log}_e\left[f(r_i)/f(r_j)\right]$$
$$- (w/2)\left[t_i/Q_{eff}(w,r_i) - t_j/Q_{eff}(w,r_j)\right] , \tag{24}$$

all the components are a function of frequency except the
geometrical attenuation factor, f(r), which was assumed
to be only a function of range. Violations of the fre-
quency independence of f(r) are discussed in the follow-
ing section on type of wave propagation. By differentia-
ting equation (24) with respect to frequency, the geo-
metrical attenuation factor can be removed, but first the
frequency dependence of $wt_i/\left[2Q_{eff}(w,r_i)\right]$ must be ascer-
tained. Although attenuation requires dispersion, the
variation of traveltime with frequency as measured by
changes in pulse shape is extremely small and cannot

exceed the ratio of the pulse length to the total travel-time (0.5/75.5 or 0.6 percent). Wuenschel (1965) observed two to three percent dispersion over five octaves. Between stations the variation would be proportionately less, and, for all practical purposes, traveltime can be considered frequency independent. The Q_{eff}, however, may be a significant function of frequency. If so, $1/Q_{eff}(w, r_i)$ can be conveniently expanded in a power series of frequency at the ith station as follows:

$$1/Q_{eff}(w, r_i) = \sum_{k=0}^{\infty} f^k/Q_{ki}. \qquad (25)$$

Substituting this expression into equation (24) and differentiating with respect to frequency gives

$$\frac{\partial}{\partial f} Log_e \left[A(w, r_i)/A(w, r_j) \right] =$$

$$\qquad (26)$$

$$-\pi \sum_{k=0}^{\infty} (k+1) \left[t_i f^k/Q_{ki} - t_j f^k/Q_{kj} \right].$$

The zero term of the summation corresponds to frequency independent attenuation. For frequency independent attenuation, equation (26) reduces to

$$\frac{\partial}{\partial f} \text{Log}_e \left[A(w, r_i) / A(w, r_j) \right] = -\pi \left[t_i / Q_{0i} - t_j / Q_{0j} \right]. \quad (27)$$

The frequency independent component of Q_{eff} for the material of the earth can be found from equation (27) only if it is also a constant with respect to range and thus only if $1/Q_{0j}$ equals $1/Q_{0i}$.

When the Q_{eff} is a function of time, the rate of attenuation, as observed along the surface, does not necessarily give the actual Q of the material sampled. The rate of change of the accumulated attenuation with respect to time along the surface, consequently, defines an apparent loss parameter, Q_{ap}, by the following:

$$1/Q_{ap} \Big|_{surface} = \frac{d}{dt} \left[t/Q_{eff}(w, r) \right]. \quad (28)$$

Q_{ap} is thus a function of time and position related to the attenuation structure of the earth. Since the increment was determined, for all practical purposes, by the station spacing Q_{ap} was approximated by

$$Q_{ap} \approx \Delta t / \Delta(t/Q_{eff})$$

$$(29)$$

$$= (t_i - t_j) / \left[t_i / Q_{eff}(w, r_i) - t_j / Q_{eff}(w, r_j) \right].$$

By use of equations (25) and (26), equation (29) becomes

$$Q_{ap} = -\pi(t_i - t_j) / \left\{ \frac{\partial}{\partial f} \text{Log}_e \left[A(w, r_i) / A(w, r_j) \right] \right. \qquad (30)$$

$$\left. - \pi \sum_{k=o}^{\infty} k \left[t_i f^k / Q_{ki} - t_j f^k / Q_{kj} \right] \right\}$$

$$Q_{ap} = -\pi(t_i - t_j) / \frac{\partial}{\partial f} \text{Log}_e \left[A(w, r_i) / A(w, r_j) \right] , \quad k=o.$$

For frequency independent attenuation, $k=0$, Q_{ap} gives the same value as that obtained by assuming the Q_{eff} to be a constant with respect to position in equation (27). For stations that are close together, both the numerator and denominator of equation (30) are small. Consequently, slight changes in the Q_{eff} or noise in the spectra can cause large variations in Q_{ap}.

In the above development of a linear theory of attenuation, three conceptually different specific dissipation functions are defined. The first, $1/Q(w,x,y,z)$ or $1/Q$, refers to the specific dissipation function at a given point in a medium. The second, $1/Q_{eff}(w,r)$ or $1/Q_{eff}$, refers to the averaged or effective specific dissipation function calculated over an entire propagation path to a range r. The third, $1/Q_{ap}(w,r)$ or $1/Q_{ap}$,

refers to the apparent specific dissipation function which
is observed along the surface. In theory the frequency
dependence of these functions can be obtained from ob-
served data with the equations previously developed.
However, in this thesis only the frequency independent
components of the specific dissipation functions are cal-
culated.

All possible Q_{ap} values, according to the frequency
independent form of equation (30), were calculated for
the GNOME and SHOAL refraction lines at 5.0 $\pm$ 0.5 and
4.0 $\pm$ 0.5 cps, respectively. The results are shown in
Tables II-a and II-b. The values along the diagonal were

TABLE II-a. Q_{ap} VALUES AT 5 CPS, <u>GNOME</u>.

<u>Range</u>	Station:	Quebec	Tango	Lima	India	Kilo
155	Sierra	−86	−285	1644	13245	231
177	Quebec	−	165	114	232	148
193	Tango		−	68	290	144
212	Lima			−	2820	112
238	India				−	124
355	Kilo					−

TABLE II-b. Q_{ap} VALUES AT 4 CPS, <u>SHOAL</u>.

Range	Station:	Tango	Romeo	Quebec	Kilo	Juliet	India	Hotel
154	Papa	-37	-73	278	167	1124	203	131
200	Tango	-	-139	248	79	185	107	85
282	Romeo		-	36	38	85	63	56
325	Quebec			-	38	148	76	62
409	Kilo				-	-39	473	95
455	Juliet					-	32	34
500	India						-	35
544	Hotel							-

calculated from adjacent stations and show the largest variations. A histogram of the values, $1/Q_{ap}$, adapted from Table II-a and II-b is shown in Figure 7. The $1/Q_{ap}$ values computed using station Sierra, GNOME, were not included since the data for this station appeared anomalous and may have been contaminated (Stewart and Pakiser, 1962). The peaks in the distributions give mean $1/Q_{ap}$ numbers corresponding to Q_{ap} values of 147 and 109 for GNOME and SHOAL, respectively.

When one of the arrivals is the source and the traveltime, t_j, is zero, equation (29) indicates that Q_{ap} is equal to Q_{eff}. Consequently equation (30) may
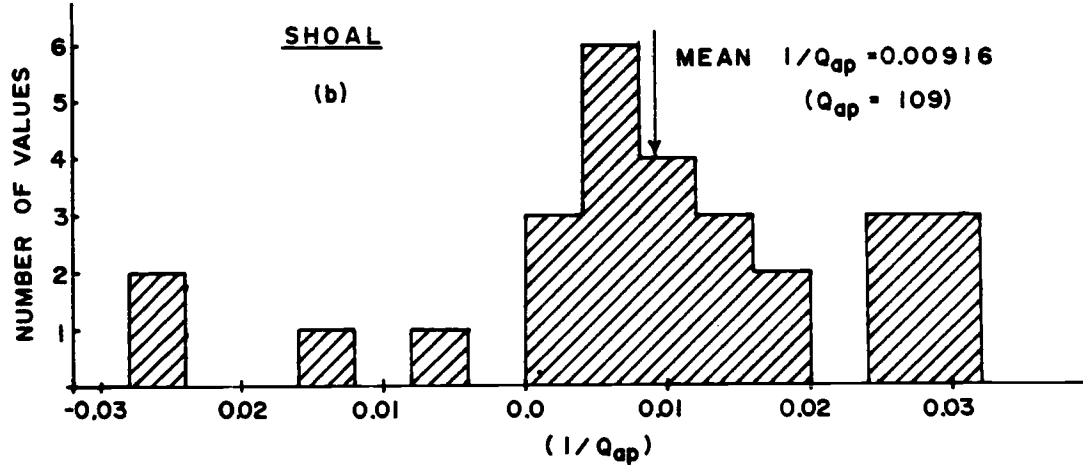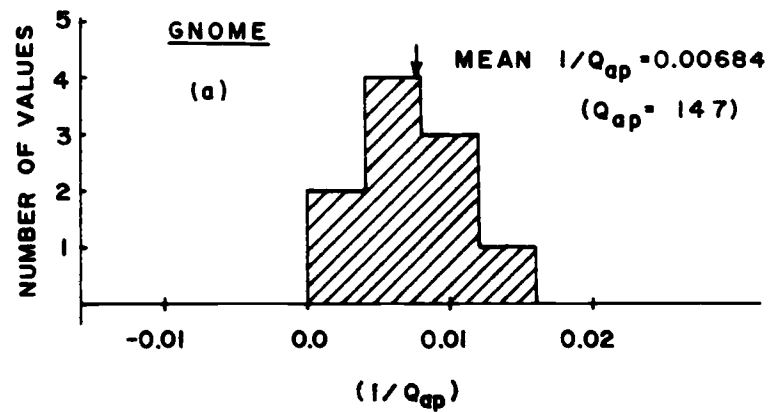
Figure 7. Histogram of $1/Q_{ap}$ values for (a) GNOME and (b) SHOAL.

also be used to calculate Q_{eff} from the source to each
station. The Q_{eff} values are presented in Tables III-a
and III-b for a set of appropriate frequencies. The Q_{eff}

TABLE III-a. Q_{eff} VALUES, <u>GNOME</u>.

f	Sierra	Quebec	Tango	Lima	India	Kilo
5 cps	1531	-1439	-5973	1557	2164	401
6 cps	497	716	731	560	463	218
7 cps	301	267	297	342	237	-
8 cps	285	162	197	280	156	-

TABLE III-b. Q_{eff} VALUES, <u>SHOAL</u>.

f	Papa	Tango	Romeo	Quebec	Kilo	Juliet	India	Hotel
4 cps	448	-376	-262	-2633	233	696	255	174
5 cps	-474	-344	-305	2410	-	-	-	-
6 cps	452	2242	1403	148	-	-	-	-

values show considerable scatter and unrealistic negative
values which indicate that the sources used may not be
appropriate for equation (30). Indeed, factors associa-
ted with the severe geometrical attenuation near the
source, interfering arrivals such as the surface reflec-
tion, and wave propagation along a continuous refraction

are not included in the sources used but do affect the

distant recordings. The measurement of Q_{ap}, however, is

not similarly affected since these factors are common to

all the distant recordings and tend to cancel out. Theo-

retically, the difference in the slope of the logarithm

of the spectra between the source and the distant record-

ing stations increases with both frequency and range.

Consequently, the inaccuracy in the Q_{eff} due to errors in

the source spectrum should decrease with increased range

and frequency and should approach the correct values

asymptotically. In actuality, however, the measurement

of the slopes is limited by noise and low relative ampli-

tude at increased ranges and frequencies. Since the Q_{eff}

values given for the greatest ranges and frequencies in

Tables III-a and III-b are the only values which corres-

pond to the mean $1/Q_{ap}$ values, the source spectra are

probably inappropriate for use in equation (30) for the

purpose of this research.

C) <u>Least-square Q_{ap}</u>. - Equation (30) can be

written as

$$\frac{\partial}{\partial f} \text{Log}_e \left[A(w, r_i) \right] = \left\{ \frac{\partial}{\partial f} \text{Log}_e \left[A(w, r_j) \right] \right.$$

$$\left. + t_j / Q_{ap} \right\} - t_i / Q_{ap}. \quad (31)$$

This is a convenient form for calculating the best value of Q_{ap} in the least-squares sense. The slope of the best fitting straight line through a plot of the measured values of traveltime and the gradients of the logarithms of the spectra yields the least-square Q_{ap}. Plots of the data and the straight lines fitted by the method of least squares are given in Figure 8. The best values of Q_{ap} are most likely 169 at five cps for GNOME and 116 at four cps for SHOAL since the distribution of the spectral peaks center about these frequencies. This choice of best Q_{ap} is supported also by the standard deviations, although the significance of the standard deviations for so few data points is questionable. Some scatter in the data about the least-square fit is to be expected from the variation of attenuation with depth, surface layering effects and interfering arrivals. Consequently, the uncertainties of the resulting Q_{ap} values are a peculiarity of the structures along each of the refraction lines and are not necessarily indicative of the precision of the
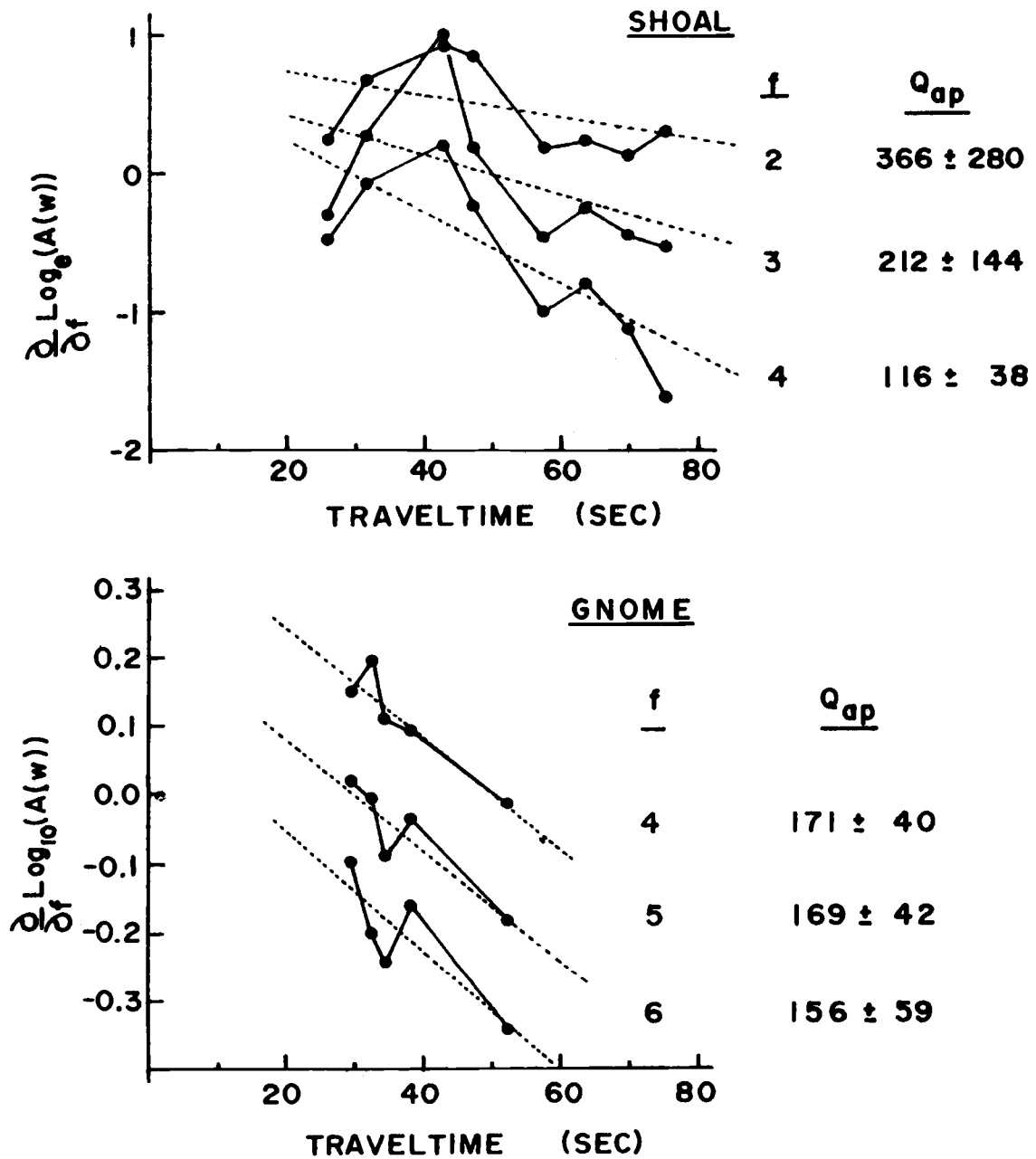
Figure 8. Q_{ap} values determined from straight lines
fitted to a plot of spectral gradient versus
traveltime by the method of least squares.

measurements.

D) <u>Total amplitude attenuation</u>. - Only the slopes

of the spectra were considered in calculating the Q_{ap},

Q_{eff} and least-square Q_{ap} values. Equation (23), however,

includes terms involving, in addition to exponential at-

tenuation, the geometrical attenuation and observed am-

plitudes. The geometrical attenuation, which has been

assumed frequency independent, theoretically can be cal-

culated from the depth versus velocity curve, but this

determination is very sensitive to slight variations in

the gradient which cannot be measured independently.

Consequently, the geometrical spreading was approximated

by r^{-n} and equation (24) is written as

$$\text{Log}_e \left[A(w, r_i) / A(w, r_j) \right] = \text{Log}_e \left[r_i^{-n} / r_j^{-n} \right]$$

$$- \pi f t_i / Q_{eff}(w, r_i) + \pi f t_j / Q_{eff}(w, r_j). \qquad (32)$$

Then by substituting equation (29) into (32) and separa-

ting the products within the logarithms, equation (32)

becomes

$$\text{Log}_e\left[A(w, r_i) \; r_i^n\right] = \left\{\text{Log}_e\left[A(w, r_j) \; r_j^n\right]\right.$$

$$\left.+ \; \pi f t_j / Q_{ap}\right\} \; - \; \pi f t_i / Q_{ap}. \qquad (33)$$

Using the observed values of A, r, and t, the method of least squares was used to calculate the best value of $\pi f / Q_{ap}$ corresponding to chosen values of n. Values of n equal to 0.5, 1.0, and 2.0 correspond to cylindrical, spherical, and head-wave geometrical attenuation, respectively. Q_{ap} values compiled for data from GNOME and SHOAL are shown in Table IV. Since geometrical spreading

TABLE IV. TOTAL AMPLITUDE ATTENUATION,

GEOMETRICAL AND ABSORPTIVE.

n	GNOME (4 cps) $(1.61/Q_{ap}) \times 10^{-3}$	Q_{ap}	SHOAL (4 cps) $(1.61/Q_{ap}) \times 10^{-3}$	Q_{ap}	
0.50	10.1 ± 4.4	159	12.2 ± 2.6	132	cylindrical
0.75	9.0 ± 4.4	178	11.4 ± 2.6	141	
1.00	7.9 ± 4.4	203	10.6 ± 2.7	152	spherical
1.25	6.8 ± 4.4	236	9.8 ± 2.7	164	
1.50	5.7 ± 4.4	281	9.3 ± 2.7	178	
1.75	4.6 ± 4.4	348	8.2 ± 2.8	195	
2.00	3.5 ± 4.3	457	7.4 ± 2.8	216	head wave

near the source and boundary losses along the propagation path were not estimated, the expression in brackets, equation (33), cannot be meaningfully related to the source by setting t_j equal to zero. The spectrally determined least-square Q_{ap} values of 169 and 116 for GNOME and SHOAL, respectively, indicate a value of n slightly more than 0.5 for GNOME and slightly less than 0.5 for SHOAL. A value of n approximately equal to 0.5, cylindrical spreading, is also obtained from independent theoretical estimates of geometrical atteunation for the velocity structures of the GNOME (Appendix II) and SHOAL (Appendix III) refraction lines. Consequently, a geometrical attenuation proportional to approximately $r^{-0.5}$ is indicated by both theoretical estimates from the velocity structures and attenuation measurements.

E) <u>Inversion of</u> Q_{ap}. - The Q_{ap} and Q_{eff} observed along the surface is directly related to the attenuation structure of the earth along the propagation path. Because a variety of factors contribute to exponential attenuation, it is undoubtedly a complicated function of both depth and range. However, factors which contribute significantly to the mechanisms of absorptive attenuation

(such as temperature, mineral composition, grain size, fluid content, and compaction) also contribute to other parameters of the crust and upper mantle (such as velocity and density). These parameters have been observed to vary with depth. In addition, frequency-dependent scattering mechanisms are probably associated with irregularities both along the boundaries between two velocity layers and near changes in the velocity gradient. Since the observed parameters (such as velocity and density) are determined by the same factors that contribute to absorptive attenuation, the depth variation of attenuation is probably more pronounced than its lateral variation.

The assumption that the attenuation structure consists only of horizontal layers of constant Q allows the index of accumulated attenuation, $K(w,r)$, of equation (21), to be expressed as a sum of the integrals through each of the layers. For N layers of penetration along the propagation path to the range r_i, the expression is

$$K(w,r_i) = \sum_{j=1}^{N} \frac{2}{Q_j} \int \frac{ds}{c} \qquad (34)$$

$$K_i = \sum_{j=1}^{N} t_{ij}/Q_j$$

where t_{ij} is the traveltime through the jth layer and

Q_j is the Q of the jth layer. The solution for $1/Q_j$ is

$$1/Q_j = \sum_{i=1}^{N} (t_{ij})^{-1} K_i. \qquad (35)$$

Care must be taken to choose the Q layering to give the

different travelpaths the greatest independence. Other-

wise, the matrix t_{ij} will approach singularity. The

layering that accomplishes this objective best is deter-

mined by the maximum depth of penetration of the rays.

Since, for this case, t_{ij} equals zero for j greater than

i, the matrix in equation (34) is triangular and its

inversion is simplified.

The quantities which must be measured are the matrix

t_{ij} and $K(w,r_i)$. In order to determine the time matrix,

t_{ij}, the velocity structures for GNOME and SHOAL, Figure

6, were used in a ray tracing computer program. The

thicknesses and depths for the layers of constant Q were

determined from the maximum depth of penetration of the

ray to each station. Then the matrix t_{ij} was determined by calculating the traveltime through the jth layer on the propagation path to the ith station. However, the total attenuation values, $K(w, r_i)$, are uncertain by some constant value unless the source is known or the value at one station can be estimated. For this study, because the sources apparently were not appropriate as indicated by the Q_{eff} values, values of Q_{eff} of 200 to Quebec, GNOME, and 135 to Quebec, SHOAL, were assumed. An improper choice of Q_{eff} would add a constant to the measured K values. The stations chosen exhibited both high-frequency character and a distinct first arrival. For GNOME, the values of K were calculated from the Q_{ap} values, Table II-a. For SHOAL, they were determined by averaging the K values calculated from the Q_{ap} values, Table II-b, and the K values estimated by comparing the observed waveforms to theoretically attenuated waveforms. These values are presented in Table V. The solutions for the attenuation values, $1/Q_j$, are plotted as a function of depth along with the velocity-depth profiles for comparison in Figures 9a and 9b.
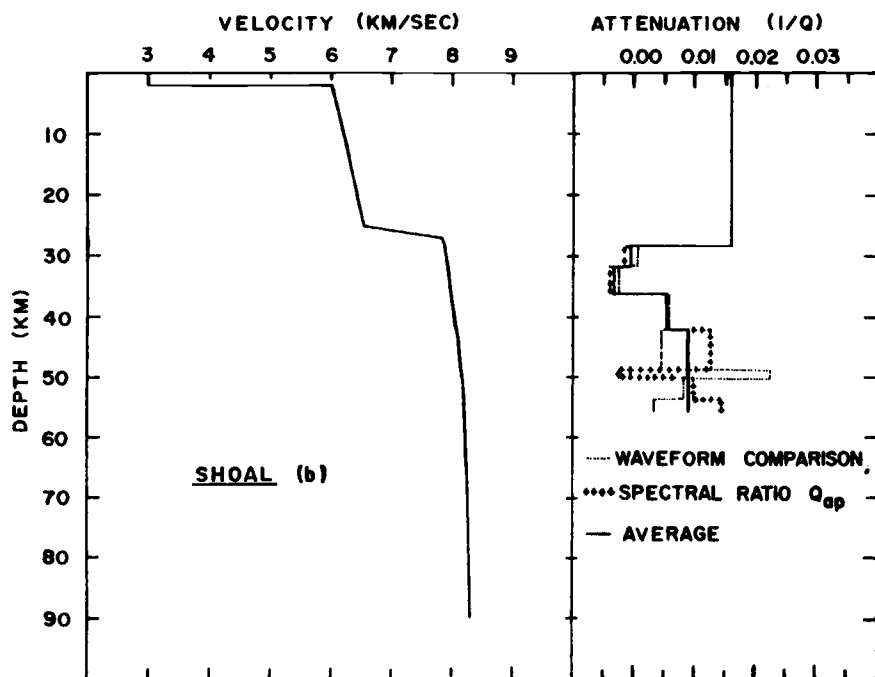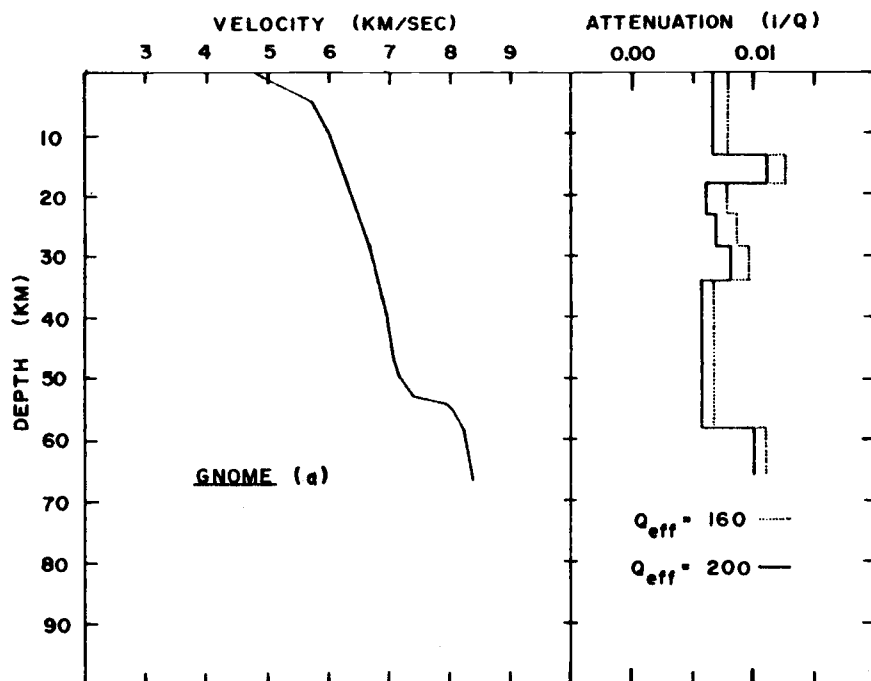
Figure 9. Velocity versus depth and attenuation versus depth profiles: (a) GNOME and (b) SHOAL.

TABLE V. MEASURED VALUES OF K.

SHOAL	K (Waveform)	K (Q_{ap})	average	GNOME	K (Q_{ap})
Papa	.40	.427	.41	Papa	.142
Tango	.30	.286	.29	Sierra	.191
Romeo	.23	.204	.215	Quebec	.146 assumed
Quebec	.35 assumed			Tango	.165
Kilo	.40	.620	.51	Lima	.191
Juliet	.65	.460	.55	India	.187
India	.60	.645	.62	Kilo	.299
Hotel	.55	.800	.675		
mean variation $\pm$ .055					

Apparently the accuracy of the measurements of K is
a critical factor since the trends which appear to exist
in the attenuation, 1/Q, versus depth structures are
associated with considerable scatter and the existence of
unrealistic negative values. The solution for an assumed
Q_{eff} of 160 to station Quebec, GNOME, in Figure 9a, how-
ever, shows that the trends are unaffected by an inappro-
priate choice of Q_{eff}. The SHOAL line, Figure 9b, shows
high attenuation at and above the Moho. Below the Moho
the attenuation at first decreases sharply and then in-
creases. The negative attenuation values immediately

below the Moho are perhaps an indication that the high attenuation at and above the Moho is actually only limited to the region of the Moho and that the actual crustal attenuation is lower. The GNOME profile, Figure 9a, shows slightly decreasing attenuation down to the Moho where one station indicates an increase. This trend is broken by abnormally high attenuation values at 15 and 30 km. These may be associated with some unidentified interference or a change in the slope of the velocity versus depth profile. Unfortunately, any measure of the actual values of attenuation, 1/Q, can be no more certain than the values of Q_{ap}.

Types of wave propagation

The frequency dependence of the geometrical attenuation term, f(r), and the existence of different types of wave propagation (head waves, continuous refractions, or multiply reflected waves) depends entirely on the crustal structure and the velocity-depth function. Theoretical analyses for more than a few constant velocity layers or a slight velocity gradient are rather complex and only the simplest cases have been solved completely.

The propagation of seismic waves from a local source in a low-velocity layer over a high-velocity medium has been described theoretically, notably by Cagniard (1962), Zvolinskii (1957, 1958), and Heelan (1953). The wave striking the boundary at the critical angle generates a head wave system which propagates along the boundary with the higher compressional wave velocity and radiates energy into the low-velocity medium in the form of shear and compressional waves and into the high-velocity medium in the form of shear waves only. Zvolinskii (1957, 1958), using a planewave approximation, obtained an expression for the amplitude and particle velocity, $\dot{q}$, of the compressional head wave at large distances given by

$$\dot{q} = A\gamma(1-\gamma^2)^{-\frac{1}{2}} \frac{1}{r^{\frac{1}{2}} L^{3/2}} \phi'(\tau) \tag{36}$$

where: $\phi'(\tau)$ = reduced velocity potential;

$(r^{\frac{1}{2}} L^{3/2})^{-1}$ = geometrical attenuation for large r;

L = glide distance, distance of critical refraction; and

$A\gamma(1-\gamma^2)^{-\frac{1}{2}}$ = head wave amplitude coefficient.

Neither the amplitude coefficient nor the geometrical

attenuation term directly affects the waveform. The waveform is entirely determined by the reduced velocity potential. The waveform of the direct arrival (see equation (8)) is determined, on the other hand, by

$$v(\tau) = - \frac{\partial}{\partial r} \left[\phi'(\tau)/r \right]$$

$$= \frac{\phi''(\tau)}{rc} + \frac{\phi'(\tau)}{r^2} \tag{37}$$

and for large r

$$\cong \frac{\phi''(\tau)}{rc} .$$

The waveform of the direct wave is therefore the reduced time derivative of the waveform of the head wave, or conversely, the integral of the direct wave gives the waveform of the head wave (Berg and Long, 1966). In the frequency domain the spectrum of the head wave, $A_h(w)$, is related to the spectrum of the direct wave, $A_d(w)$, by

$$A_d(w) = iwA_h(w) . \tag{38}$$

Equation (38) provides a means of distinguishing between a head wave and a direct wave if both types of wave propagation are represented in a refraction line. The distinction is important because it implies two different concepts of wave propagation. Where head waves are

identified, the propagation is along smooth boundaries in a medium of constant velocity layers. If direct waves are observed, the propagation is along a curved ray path, a continuous refraction, and the ray is returned to the surface by a positive velocity gradient.

O'Brien, (1955) showed that head waves could be generated in a model. The head waves he observed showed the proper frequencies with respect to the direct arrivals. There is, however, some question as to whether head waves are actually observed in refraction studies of the earth's crust, even though the analysis techniques applied usually assume a constant velocity model. If direct waves are observed, more complicated methods involving curved raypaths should be employed. The results may or may not differ appreciably.

The arrivals along the GNOME refraction line, which have been identified as direct arrivals (Laun, 1965; Berg and Long, 1966) showed a gradual increase in period which was attributed to attenuation. SHOAL, however, showed a variation in waveform and frequency content which could possibly be attributed to the presence of both the head and direct type of wave propagation. The arrivals at stations Tango, Sierra, Romeo, and Quebec showed

significantly higher frequencies than the others. The

mixed type of wave propagation interpretation for SHOAL

(Berg and Long, 1966) would classify the high-frequency

arrivals as direct arrivals and the remaining low-

frequency arrivals as head waves. Figure 10 shows the

theoretical head waveform calculated by integrating the

direct waveform of station Romeo. The comparison of the

theoretical head waveform to the arrivals at stations

Kilo and Hotel, Figure 10, is favorable and only slight

attenuation is indicated.

The measurements of Q_{ap} made by comparing a head

wave to a direct wave must account for the effects of

their respective interpretations. Table VI shows the Q_{ap}

values of Table II-b adjusted for the interpretation by

Berg and Long (1966). An average increase in Q_{ap} by

approximately one third is indicated. The adjusted mean

value of $1/Q_{ap}$ indicates a Q_{ap} of 120. Table IV indi-

cates that even a Q_{ap} as high as 140 would require a

geometrical attenuation factor of r^{-n} with n equal to

0.75. A value of n greater than two would be required to

show head wave geometrical attenuation. With n equal to

two, an extrapolation of the amplitudes at ranges greater
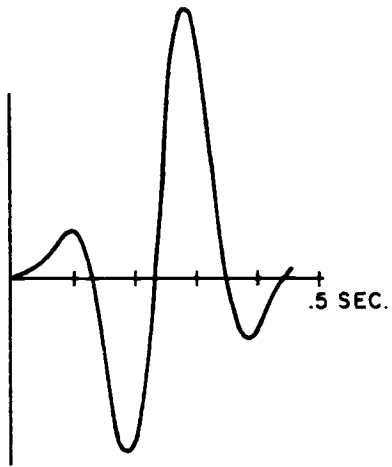
a. RANGE: 282 km
   TRACE: 3
   DIRECT WAVE
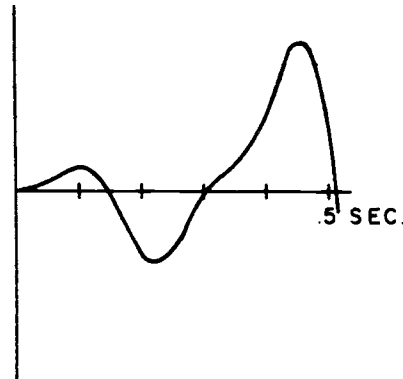
b. RANGE: 409 km
   TRACE: 1
   HEAD WAVE
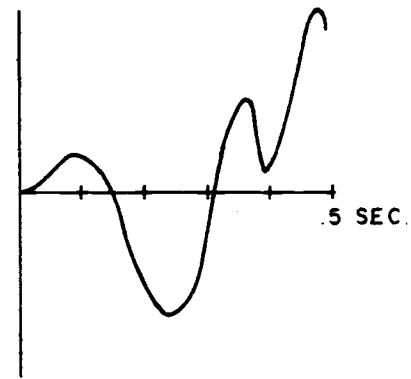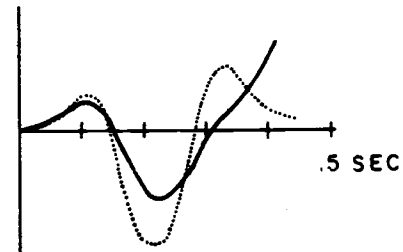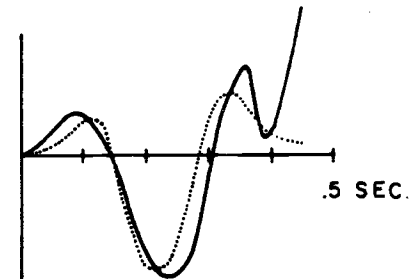
c. RANGE: 544 km
   TRACE: 1
   HEAD WAVE
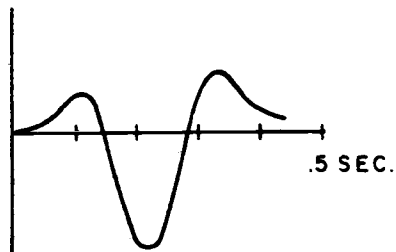
d. INTEGRATION OF DIRECT
   WAVE ARRIVAL OF
   FIGURE 4a

e. COMPARISON OF FIGURE 4d
   (DOTTED) AND 4b (SOLID)
   FOR ARBITRARY AMPLITUDES

f. COMPARISON OF FIGURE 4d
   (DOTTED) AND 4c (SOLID)
   FOR ARBITRARY AMPLITUDES

Figure 10.   Comparison of theoretical head wave to observed arrivals (after
             Berg and Long, 1966).

TABLE VI. Q_{ap} AT 4 CPS, ADJUSTED FOR HEAD OR

DIRECT WAVE INTERPRETATION, <u>SHOAL</u>.

	Papa H	Tango D	Romeo D	Quebec D	Kilo H	Juliet H	India H	Hotel H
Papa H	–	<u>-83</u>	<u>-114</u>	<u>6960</u>	167	1124	203	131
Tango D		–	-139	248	<u>104</u>	<u>340</u>	<u>138</u>	<u>101</u>
Romeo D			–	36	<u>47</u>	124	<u>77</u>	<u>65</u>
Quebec D				–	<u>54</u>	<u>535</u>	103	<u>75</u>
Kilo H					–	-39	473	95
Juliet H						–	32	34
India H							–	35

<u>000</u> adjusted values, D = direct, H = head

than 350 km back to a range of 200 km indicates that a head wave should exist at 200 km with an amplitude greater than 0.0055 cm/sec. The observed first arrival, however, is the largest immediate compressional arrival at a range of 200 km and has an amplitude less than 0.0017 cm/sec. Thus the head wave interpretation cannot satisfy both the spectral ratio attenuation measurements and the observed amplitudes.

An alternative to the head wave interpretation is direct wave propagation and exponential attenuation with Q_{eff} which varies with range. To show that exponential

attenuation can explain both the amplitude and waveform measurements, the arrival at station Romeo, SHOAL, has been propagated out to 520 km by using a causal attenuation operator, equation (19), (Futterman, 1962). Figure 11 shows the operator for t/Q_{eff} equal to 0.1, and the progressive change in the character of the arrival at station Romeo as it propagates out to 520 km. The comparison with station Hotel at 550 km is shown in Figure 11 also, and confirms that attenuation can account for both the amplitude and waveform variation. Whether head waves have been observed in crustal studies is a question that will require further searching to answer. They are not apparently observed as first arrivals along either the GNOME or SHOAL refraction lines.

Where velocity gradients exist, the wave equation does not easily separate (Hook, 1965), and exact solutions are very difficult. For a slowly varying positive velocity gradient, nevertheless, the geometrical optics approximation to the wave equation can be used. Snell's law is then applicable and curved raypath techniques can be used to find traveltimes, structures, and most amplitudes. Waveform distortions due to secondary or multiple arrivals can be predicted by the geometrical

CAUSAL ATTENUATION OPERATOR

(FUTTERMAN, 1966)

$t/Q_{eff} = 0.1$

0   I SEC

ROMEO SHOAL

(282 KM)

4×10^{-4}
$\frac{cm}{sec}$

0   I SEC

ROMEO PROPAGATED 10 SEC

AT Q = 100 ($\approx$ 360 KM)

4×10^{-4}
$\frac{cm}{sec}$

0   I SEC

ROMEO PROPAGATED 20 SEC

AT Q = 100 ($\approx$ 440 KM)

4×10^{-5}
$\frac{cm}{sec}$

0   I SEC

ROMEO PROPAGATED 30 SEC

AT Q = 100 ($\approx$ 520 KM)

4×10^{-5}
$\frac{cm}{sec}$

0   I SEC

HOTEL SHOAL

(550 KM)

1×10^{-5}
$\frac{cm}{sec}$
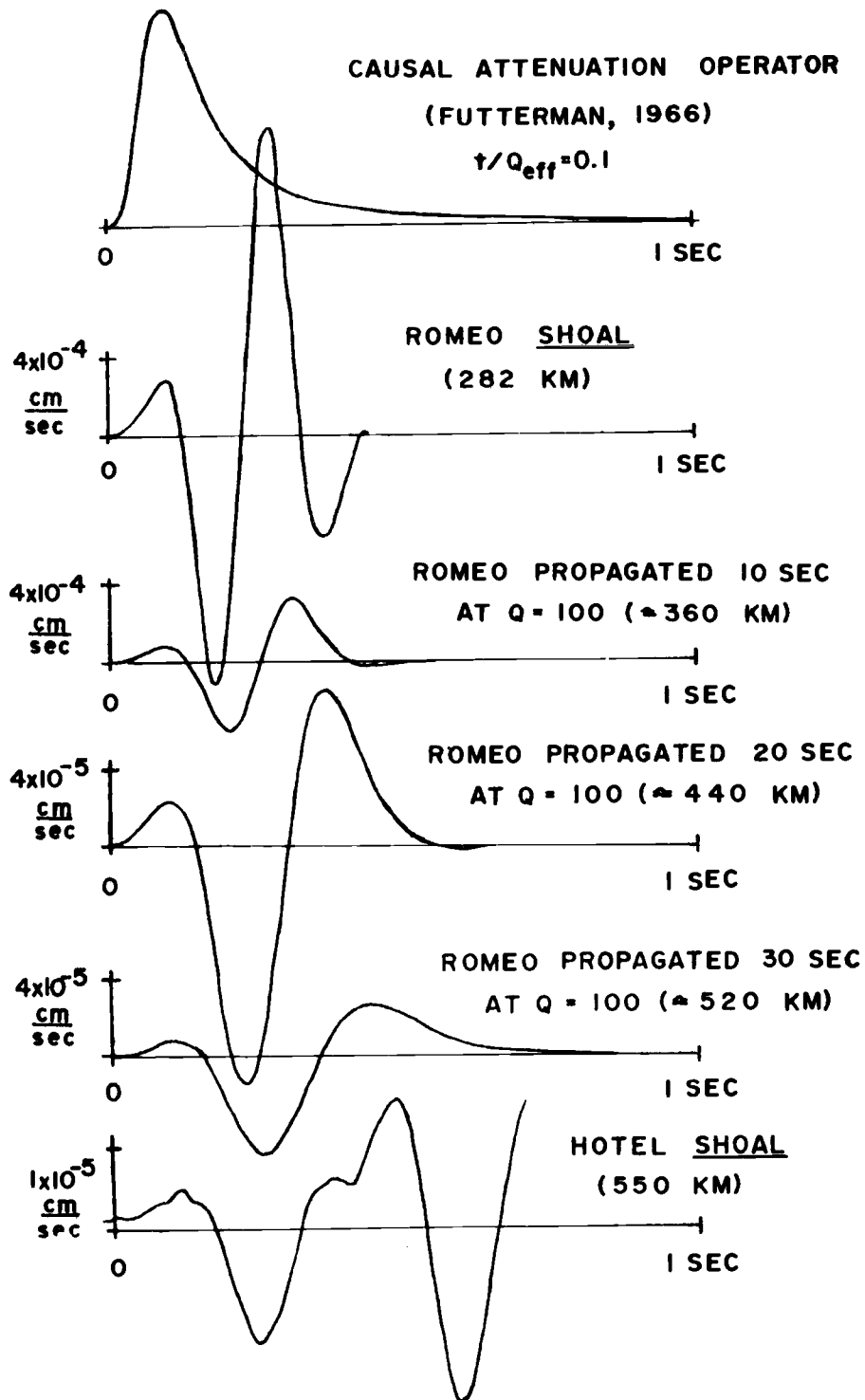
0   I SEC

Figure 11. Effect of a causal attenuation operator.

optics approximation. However, when the velocity varies appreciably within one wavelength, the geometrical optics approximation cannot be used to determine pulse distortions.

When a wave is turned back to the surface by a positive velocity gradient its pulse shape is undoubtedly altered. The approximate solution near the turning point suggests that a 90° change in phase normally takes place (Brekhovskikh, 1960, p. 213), but its exact nature may depend on the velocity gradient. There may also be a frequency dependent amplitude term associated with various velocity gradients. For the arrivals along the GNOME and SHOAL refraction lines, which are continuous refractions, only changes in character with distance were important and the effect on the wave at the turning point should be similar for all ranges.

Below the Moho at a depth of about 65 km the velocity is believed either to decrease or to become constant. The raypaths of many of the arrivals approach this depth at their apex, and the total thickness involved in the raypath below the Moho is less than 15 km for GNOME and 30 km for SHOAL. The low frequencies (below one cps) with wavelengths greater than eight km

could leak energy into the low or constant velocity zone

below 65 km (Archambeau, Flinn, and Lambert, 1966). The

frequencies primarily studied were, however, between

three and six cps with wavelengths of 2.6 and 1.3 km,

respectively, and this effect would be slight if measur-

able at all. In comparison to the overwhelming effect of

exponential attenuation the effect of a velocity gradient

on character of the pulse is probably not significant.

The two prominent boundaries, the free surface and

the Moho, in combination with a positive velocity gra-

dient beneath them, effectively create two energy chan-

nels. In these channels continuous refractions are re-

peatedly reflected downward on striking the free surface

or the Moho from below. The upper channel, the crustal

channel, is responsible for the $\overline{P}$ and P_g arrivals des-

cribed by Ryall and Stewart (1963). The lower channel

is responsible for the Moho arrival, P_n and some of the

immediate secondary arrivals. The major portion of the

arrivals associated with both channels occur as secondary

arrivals, and are described in Appendix III.

The energy channel created by the Moho and the

positive velocity gradient below offers an alternate

concept of the P_n arrival which can explain the observed

geometrical spreading factor estimated at $r^{0.5}$ and the

distance to which it propagates. Complexities in the am-

plitude can arise from a number of factors including: a

strong dependence of the reflection and refraction co-

efficients on angle of incidence; the velocity contrast

at the Moho; variations in dip or velocity at the Moho;

and focusing caused by variations in the velocity gra-

dient below the Moho. In particular, the constant or de-

creasing velocity below 60 km depth would attenuate the

direct arrival at greater ranges and cause the doubly

refracted arrival to appear larger and to interfere with

the measurement of the first arrival. All of the above

factors, consequently, can contribute to the complexity

of the arrivals beyond 350 km.

SOURCE ENERGY TRANSMISSION

In the spectral analysis, frequencies with amplitudes less than one tenth the peak spectral amplitude often contain a large percentage of noise and usually are not directly related to the source. Using this observation as a criterion of reliability together with the combined filtering of instrument response and exponential attenuation, a functional relation between the highest reliable frequency, the Q_{eff}, and time or range was developed. These functions for Q_{eff} values of 100 and 200 are plotted in Figure 12. The low-frequency cutoff is basically determined at one cps by the instrument response.

The curves of Figure 12 apply to an impulsive type source. The source spectra for GNOME and SHOAL, however, peak at 5 and 3.5 cps respectively and are thus somewhat deficient in both low- and high-frequency energy. A deficiency of source energy at the low frequencies tends to shift the curves in Figure 12 toward slightly higher frequencies at greater ranges. A deficiency in source-related energy at high frequencies shifts the curves, particularly at close ranges, toward lower frequencies.
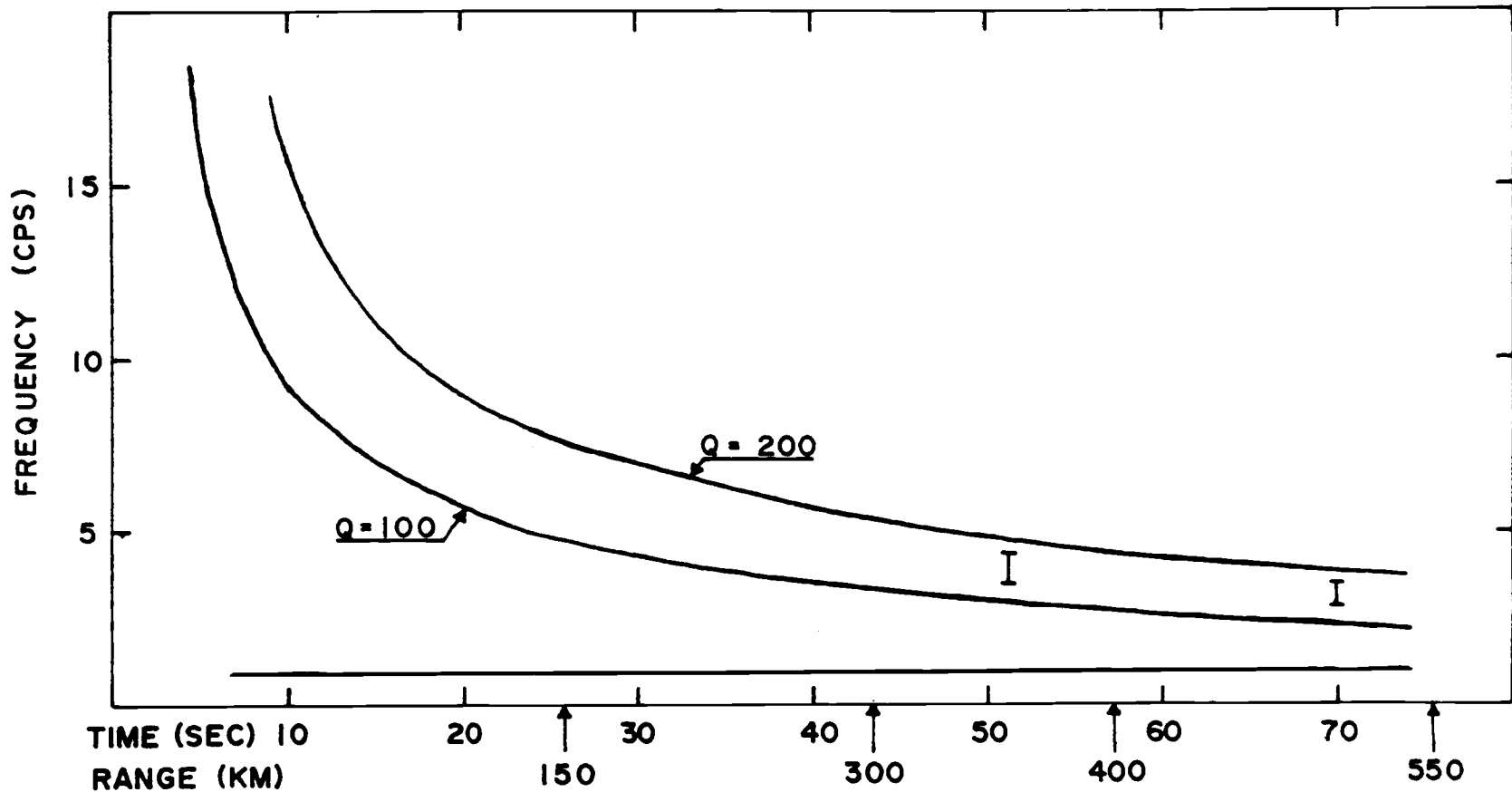
Figure 12.   Highest reliable frequency versus range.

Consequently, a source spectrum peaking in energy between

two and five cps, as do the GNOME and SHOAL spectra, will

flatten the curves in Figure 12 and increase the range

over which pulses with similar reliable frequencies can

be observed. In addition, surface effects and other con-

taminations can cause variations in the spectra which can

alter the highest reliable frequencies significantly,

particularly beyond 200 km. An estimate of these varia-

tions can be made from the measured variations in K of

± 0.055, Table V, or the variations in apparent frequency

due to surface effects in Figure 5 of ± 0.5 cps. Esti-

mates of these variations in terms of Q_{eff} or cps are

plotted at 50 and 70 seconds in Figure 12.

The most significant implication of Figure 12 is

that a pulse recorded at 150 km with a Q_{eff} of 100 can

be very similar to a pulse recorded at 400 km with a Q_{eff}

of 200. In both cases source information above 4.5 cps

is severely attenuated and unreliable. A range of almost

250 km for similar pulses is possible when Q_{eff} varies

between 100 and 200 as a function of range. Surface

effects and contamination would extend the range over

which similar pulses may be recorded even further.

Clearly, a source without significant high-frequency

energy could produce waveforms at ranges from 100 to 600

km with spectra essentially independent of range. If, on

the other hand, the variation of Q_{eff} with range were

known, the uncertainty in the maximum reliable frequency

would depend primarily on surface effects and contamina-

tion. The range over which similar pulses could be ob-

served would then depend on the Q_{eff} function. Neverthe-

less, Figure 12 indicates that for a range independent

Q_{eff}, surface effects and contamination could cause simi-

lar pulses to be observed over a range of 100 km at 30

sec and that this range increases with distance from the

source.

The effect of attenuation on amplitude is just as

pronounced as it is on waveform. The solid lines in

Figure 13 show the amplitude attenuation for the combined

effects of geometrical attenuation proportional to $r^{-0.5}$

and exponential attenuation at 3.5 cps for Q_{eff} values

of 100 and 200. The two solid lines also indicate the

variation in amplitude than can result if Q_{eff} varies

between 100 and 200 with range. Both GNOME and SHOAL

show geometrical attenuation proportional to $r^{-0.5}$ and

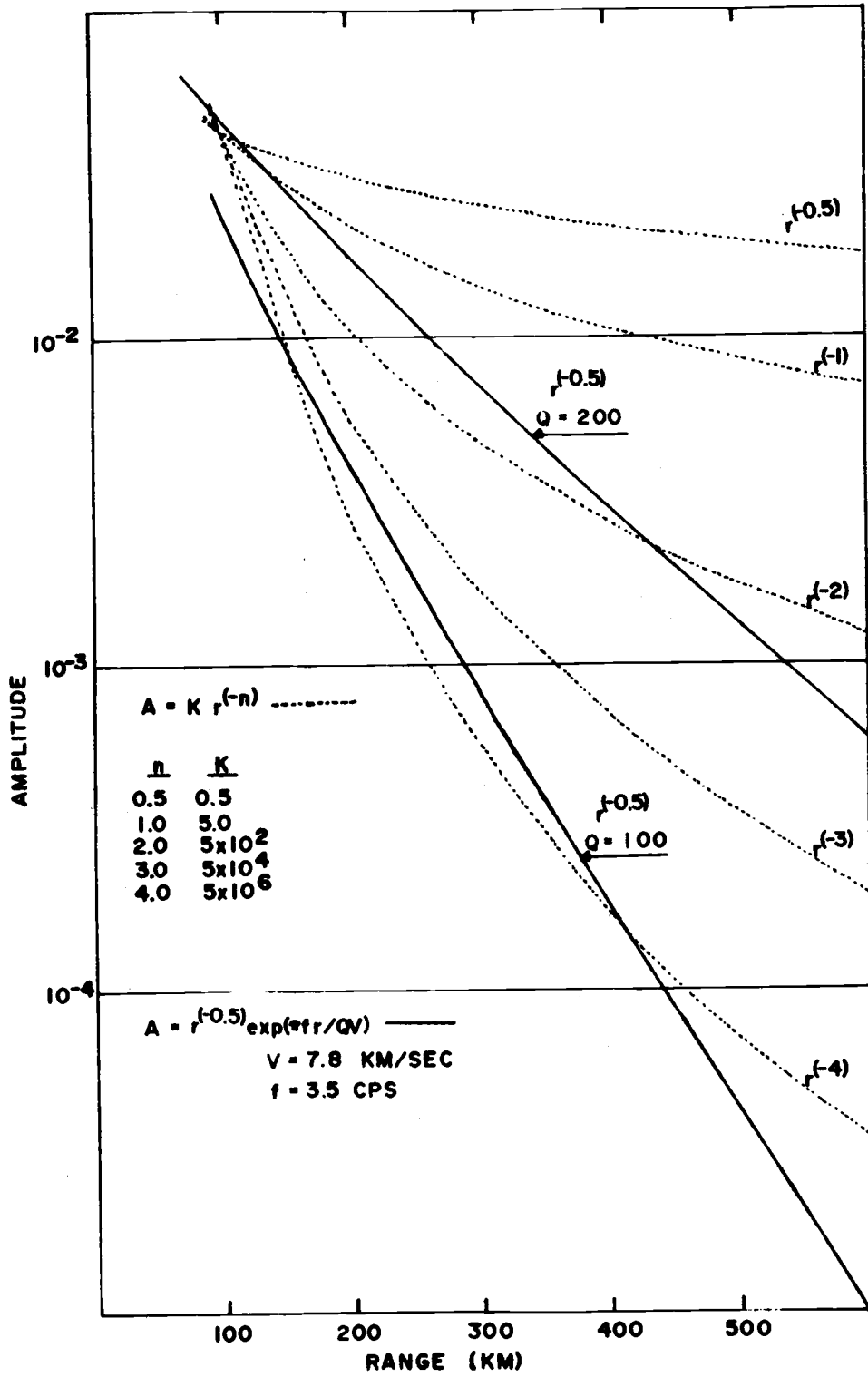Q_{ap} values between 100 and 200. The actual geometrical

Figure 13. Expected amplitude variation with distance.

attenuation, however, depends on the velocity gradient and could include focus points or shadow zones. For the GNOME and SHOAL lines, this type of variation appeared to be less than a factor of five. Attenuation within the predicted range of Q_{eff}, 100 to 200, may be approximated by amplitudes decreasing according to r^{-n}, with n varying from two to four. This includes a value of n equal to three (Romney, 1959).

In the inverse problem of estimating source character from a recording at distance, the distinction between attenuated energy and energy absent from the source is ambiguous for frequencies above the curve in Figure 12 corresponding to the minimum Q_{eff} that can be expected. Since along the GNOME and SHOAL refraction lines, Q_{ap} was primarily between 100 and 200, the ambiguity at 300 km includes all frequencies greater than 3.5 cps. These frequencies comprise a large portion of the source energy for both GNOME and SHOAL. Similarly, for a minimum Q_{eff} of 100, ranges of 100 km or less would be required, according to Figure 12, to measure reliably source energy at least to six cps. Unfortunately, the first P-wave arrivals at these ranges depend strongly on the more irregular structure of the upper crust for their

character and have not been investigated in this research.
If Q_{eff} were known and its value were greater than 100,
the range of reliable frequencies would be extended.

The amplitude curves presented in Figure 13 were
developed only for ranges from 100 to 600 km and cannot
be used to estimate the source amplitude or the amplitude
versus distance function for ranges less than 100 km.
Nevertheless, Figure 13 does give a source-amplitude un-
certainty factor when Q_{eff} is known only to be between
100 and 200. At 300 km the uncertainty factor is close
to one order of magnitude and increases with range. If
the Q_{eff} and geometrical attenuation were known and if
source data were available to calibrate the curves in
Figure 13, the uncertainty factors could be considerably
reduced. However, surface layer effects and local struc-
tural variations could still cause appreciable uncer-
tainty. A measure for this uncertainty of $\pm$ 30 percent
is indicated by the mean standard deviation of the SHOAL
amplitudes (see Figure III-4).

The difficulties in predicting the character and
amplitude of the source pulse from the character and
amplitude of the distant arrivals are primarily a con-
sequence of regional variations in crustal structure,

Q_{eff}, and near surface structure. A knowledge of the variability of these three factors is of primary importance in defining the uncertainty of any estimate of source character and amplitude for a particular region. Determination of the variability of these factors for general application, however, would require studies including many regions.

A supplemental means of reducing the ambiguities would be to calibrate each source-to-detector propagation path with an explosion that has the character of an impulse. Variations in the records of other events from the same source location could be directly related to variations in the source. This method is critically limited in that the calibration applies to only one source location and detector. It only applies to the reliable frequencies indicated in Figure 12 also. A comparison of this type was not possible with the data used in this thesis.

DISCUSSION AND CONCLUSIONS

The waveform analysis of the GNOME and SHOAL first arrivals has revealed some important effects of P-wave transmission and attenuation at ranges of 100 to 600 km. The dominant effects fall into the following generalized categories: uniform transmission effects, irregular effects, and attenuation effects. The importance of these effects is that they determine the manner and reliability with which source character and energy is propagated, and indicate the magnitude of the variations of waveform which may occur as a function of range. In the inverse problem they determine the uncertainty of any estimate of source character and magnitude from distant signals.

Uniform transmission effects

The first P-wave arrival for both GNOME and SHOAL was transmitted as a continuous refraction, even though the Moho at 55 km along the GNOME profile was 25 km deeper than along the SHOAL profile. The effect on the waveform of the first arrival of being returned by a positive velocity gradient was not considered

significant when compared to other effects. Also, for a

nearly constant gradient all the first arrivals would

have been affected similarly. The effect on the waveform

of an arrival which is returned by a positive velocity

gradient more than once was not estimated. The geometri-

cal attenuation corresponding to the continuous refrac-

tions observed along both refraction lines was approxi-

mately $r^{-0.5}$. Head waves, which have a geometrical

spreading factor of about r^{-2}, were either too small to

be observed or the boundaries were too irregular to sup-

port their propagation.

Transmission as a continuous refraction or direct

wave for the P_n arrival provides an alternative to head

wave propagation. This choice of wave type is consistent

with the computed geometrical attenuation of $r^{-0.5}$ and

the wave is probably bound to an energy channel formed

by the Moho and the positive velocity gradient below it.

The observed interfering arrivals at distances greater

than 350 km for SHOAL would represent multiply refracted

waves within the energy channel. The amplitudes of these

arrivals would depend strongly on the angle of incidence

at the Moho and on slight variations in the velocity

gradient. In particular, the constant or decreasing

velocity below a depth of 60 km would attenuate the direct arrival at greater ranges and cause the doubly refracted arrival to appear larger. These factors undoubtedly further complicated the arrivals at greater distances.

Irregular effects

Irregular effects, effects acting independently on each station, were caused primarily by seismic noise, surface layering effects, and large interfering arrivals, and were the most difficult effects to determine. High-frequency microseisms were a problem only at station Juliet, GNOME, and for the most part extraneous seismic noise was either non-existent or sufficiently suppressed by stacking the traces. Surface layering by far could have introduced the most difficult to measure and pronounced effects. In a theoretical example of a single surface layer the amplitudes varied by as much as $\pm$ 25 percent and the apparent frequency varied by as much as ± 0.5 cps, when the thickness of the surface layer was varied from 0.0 to 250 meters. This variation in frequency is equivalent to a Q_{eff} of 100 operating over a distance of about 100 km. Some first arrivals were

further contaminated by large amplitude interfering

arrivals. This appeared to be the case for the distant

arrivals along the SHOAL line. However, the effects of

most of the larger interfering arrivals could be elimina-

ted. Small amplitude interfering arrivals were hard to

identify and evaluate. The unexplained high-frequency

component at station India, SHOAL, indicated the exis-

tence of other independent effects, perhaps non-linear,

generating or selectively amplifying frequencies which

are normally attenuated.

Attenuation effects

Exponential attenuation was undoubtedly the domi-

nant distance related effect in determining waveform and

amplitude of the first arrivals. The rate of attenuation

along the surface, Q_{ap}, with least-square values of 169

and 116 for GNOME and SHOAL, respectively, accounted for

most of the amplitude decay and the decrease in peak

frequency with distance. The distribution of Q_{ap}, the

mean Q_{ap}, and the least-square Q_{ap} values indicated that

Q_{ap} ranged between 100 and 200 at ranges of 100 to 600 km

from the GNOME and SHOAL shot points. A Q_{eff} of 100

implies a functional relation between frequency and

distance in which frequencies above four cps at 150 km

and above three cps at 400 km will be less than one

tenth the peak spectral amplitude and cannot be reliably

related to the source. Q_{eff} values ranging between 100

and 200 also imply an uncertainty in amplitude at 300 km

of about one order of magnitude which increases with dis-

tance. If Q_{eff} were known for the particular region

these uncertainties would be reduced. The difference in

Q_{ap} for GNOME, 165, and SHOAL, 116, was probably due to

regional geological variations.

By assuming that attenuation was only a function of

depth, the attenuation versus depth function could be

derived from the dependence of Q_{eff} or Q_{ap} on range.

The GNOME attenuation versus depth profile indicated a

slightly decreasing attenuation down to the Moho, and

one station indicated an increase below it. The SHOAL

attenuation versus depth profile indicated an increasing

attenuation below the Moho. These trends were strongly

affected by high-attenuation layers perhaps associated

with boundaries or changes in the velocity gradient.

Further substantiation of these trends would require

station spacing more dense than in either the GNOME or

SHOAL refraction line and additional measurements in a

variety of regions.

BIBLIOGRAPHY

Archambeau, C.B., E.A. Flinn and D.G. Lambert. 1966. Detection, analysis, and interpretation of tele-seismic signals. Journal of Geophysical Research 71:3483-3501.

Berg, Joseph W., Jr. and L. Timothy Long. 1966. Characteristics of refracted arrivals of seismic waves. Journal of Geophysical Research 71:2583-2589.

Berg, Joseph W., Jr. and George E. Papageorge. 1964. Elastic displacement of primary waves from explosive sources. Bulletin of the Seismological Society of America 54:947-959.

Berg, Joseph W., Jr., Lynn D. Trembly and Philip R. Laun. 1964. Primary ground displacements and seismic energy near the GNOME explosion. Bulletin of the Seismological Society of America 54:1115-1126.

Berg, Joseph W., Jr. et al. 1960. Seismic investigation of crustal structure in the eastern part of the basin and range province. Bulletin of the Seismological Society of America 50:511-535.

Brekhovskikh, Leonid M. 1960. Waves in layered media, tr. by David Lieberman. New York, Academic. 561 p.

Cagniard, L. 1962. Reflection and refraction of progressive seismic waves, tr. by Edward A. Flinn and C. Hewitt Dix. New York, McGraw-Hill. 282 p.

Eaton, J.P. 1963. Crustal structure from San Francisco, California, to Eureka, Nevada, from seismic-refraction measurements. Journal of Geophysical Research 66:5789-5806.

Foster, Roy W. and Thomas F. Stipp. 1961. Preliminary geologic and relief map of the Precambrian rocks of New Mexico. Socorro. 8 p. (New Mexico. State Bureau of Mines and Mineral Resources, New Mexico Institute of Mining and Technology. Circular 57)

Fuchs, Karl. 1966. The transfer function for P-waves for a system consisting of a point source in a layered medium. Bulletin of the Seismological Society of America 56:75-108.

Futterman, Walter I. 1962. Dispersive body waves. Journal of Geophysical Research 67:5279-5292.

Grant, F.S. and G.F. West. 1965. Interpretation theory in applied geophysics. New York, McGraw-Hill. 582 p.

Heelan, P.A. 1953. On the theory of head waves. Geophysics 18:871-893.

Hook, J.F. 1965. Determination of inhomogeneous media for which the vector wave equation of elasticity is separable. Bulletin of the Seismological Society of America 55:975-987.

Howell, B.F., Jr. 1963. Absorption of seismic waves. Ann Arbor, University of Michigan, Institute of Science and Technology, Acoustic and Seismic Laboratory. 27 p. (VESIAC State-of-the Art Report. 5272 Contract SD-78)

Huang, Y.T. 1966. Spectral analysis of digitized seismic data. Bulletin of the Seismological Society of America 56:425-440.

Knopoff, L. 1964. Q. Reviews of Geophysics 2:625-660.

Laun, P.R. 1965. Primary seismic wave (P) at 250-350 km compared to measured wave at 0.3 km from GNOME nuclear explosion. Master's thesis. Corvallis, Oregon State University. 55 numb. leaves.

Mabey, Don R. 1960. Regional gravity survey of Nevada. U.S. Geological Survey, Professional Paper 400B: 283-285.

O'Brien, P.N.S. 1955. Model seismology, the critical refraction of elastic waves. Geophysics 20:227-242.

Officer, C.B. 1958. Introduction to the theory of sound
     transmission. New York, McGraw-Hill. 284 p.

Pakiser, L.C. 1963. Structure of the crust and upper
     mantle in the western United States. Journal of
     Geophysical Research 68:5747-5756.

Pakiser, L.C. 1965. The basalt-eclogite transformation
     and the crustal structure in the western United
     States. In: Geological survey research, 1965.
     Washington, D.C., U.S. Geological Survey. p. 1-8
     (Professional Paper 525B)

Pakiser, L.C. and J.S. Steinhart. 1964. Explosion seis-
     mology in the western hemisphere. In: Research in
     geophysics. Vol. 2. Solid earth and interface pheno-
     mena, ed. by Hugh Odishaw. Cambridge, Massachusetts
     Institute of Technology, p. 123-147.

Romney, C. 1959. Amplitudes of seismic body waves from
     underground nuclear explosions. Journal of Geo-
     physical Research 64:1489-1498.

Romney, C. et al. 1962. Travel times and amplitudes of
     principal body phases recorded from GNOME. Bulletin
     of the Seismological Society of America 52:1057-1074.

Ryall, Alan and D.J. Stuart. 1963. Traveltimes and ampli-
     tudes from nuclear explosions: Nevada test site to
     Ordway, Colorado. Journal of Geophysical Research
     68:5821-5835.

Springer, D.L. 1966. Calculation of first-zone P wave am-
     plitudes for SALMON event and for decoupled sources.
     Journal of Geophysical Research 71:3459-3467.

Stewart, S.W. and L.C. Pakiser. 1962. Crustal structure
     in eastern New Mexico interpreted from the GNOME ex-
     plosion. Bulletin of the Seismological Society of
     America 52:1017-1030.

Trembly, Lynn D. and Joseph W. Berg, Jr. 1966. Amplitudes and energies of primary seismic waves near the HARD-HAT, HAYMAKER, and SHOAL nuclear explosions. Bulletin of the Seismological Society of America 56: 643-653.

Warrick, R.E. et al. 1961. The specification and testing of a seismic-refraction system for crustal studies. Geophysics 26:820-824.

Werth, G.C., R.J. Herbst and D.L. Springer. 1962. Amplitudes of seismic arrivals from the M discontinuity. Journal of Geophysical Research 67:1587-1610.

White, J.E. 1965. Seismic waves: radiation, transmission and attenuation. New York, McGraw-Hill. 302 p.

Wuenschel, P.C. 1965. Dispersive body waves - an experimental study. Geophysics 30:539-551.

Zvolinskii, N.V. 1957. Reflected and head waves emerging at a plane interface of two elastic media, 1. Bulletin of the Academy of Science of U.S.S.R., Geophysics ser., 1957, no. 10, p. 1-21. (Translated from Izvestia Akademii Nauk S.S.S.R., ser. Geofizicheskaia)

Zvolinskii, N.V. 1958. Reflected waves and head waves arising at a plane interface between two elastic media, 2. Bulletin of the Academy of Science of the U.S.S.R., Geophysics ser., 1958, no. 1, p. 1-7. (Translated from Izvestia Akademii Nauk S.S.S.R., ser. Geofizicheskaia)

APPENDICES

APPENDIX I

Derivation of the surface layering effect

A compressional seismic pulse striking a layered free surface at normal or near normal incidence in an elastic medium converts little or no energy into other modes of propagation. Thus, only compressional waves need be considered in the derivation of the surface effect. The displacement potentials in the kth layer, ϕ_k, must satisfy the wave equation:

$$\frac{\partial^2}{\partial t^2} \phi_k = \alpha_k^2 \frac{\partial^2}{\partial x^2} \phi_k \, ,$$

where α_k is the velocity of the kth layer. In terms of the Fourier integral transform the wave equation becomes

$$\omega^2 \Phi_k + \alpha_k^2 \frac{\partial}{\partial x^2} \Phi_k = 0$$

where Φ_k is the Fourier transform of ϕ_k. The solution to the spectral form of the wave equation is

$$\Phi_k = A_k \exp\left[+\frac{\omega}{\alpha_k} x\right] + B_k \exp\left[-\frac{\omega}{\alpha_k} x\right]$$

where A_k and B_k are complex functions of ω which must be evaluated by using the three following boundary conditions

given for n layers over an infinite half space.

1. The displacement across each boundary surface

must be continuous:

$$\frac{\partial}{\partial x}\Phi_K = \frac{\partial}{\partial x}\Phi_{K+1}\bigg|_{x=h_K} , \quad K=1,2\cdots n.$$

2. The stress across each boundary surface must be

continuous:

$$\rho_K \alpha_K^2 \frac{\partial^2}{\partial x^2}\Phi_K = \rho_{K+1} \alpha_{K+1}^2 \frac{\partial^2}{\partial x^2}\Phi_{K+1}\bigg|_{x=h_K} , \quad K=1,2\cdots n,$$

where ρ_K is the density of the kth layer.

3. The stress at the free surface must be zero:

$$\rho_1 \alpha_1^2 \frac{\partial^2}{\partial x^2}\Phi_1 = 0\bigg|_{x=0}.$$

There exists, therefore, 2n+1 equations from which

any of the 2(n+1) unknown coefficients may be calculated

in terms of a known coefficient, usually the incident co-

efficient B_{n+1}. For more than one layer the analytical

solution involves considerable algebra. The solution for

digital data, however, can be handled by simply inverting

the complex coefficient matrix at discrete frequencies.

For one layer, $n=1$, the equations are

$$\begin{bmatrix} -\rho_1 \omega^2 & -\rho_1 \omega^2 & 0 \\ \frac{i}{\alpha_1}\exp[\frac{i\omega}{\alpha_1}h] & \frac{-i}{\alpha_1}\exp[\frac{-i\omega}{\alpha_1}h] & \frac{-i}{\alpha_2}\exp[\frac{i\omega}{\alpha_2}h] \\ -\rho_1\exp[\frac{i\omega}{\alpha_1}h] & -\rho_1\exp[\frac{-i\omega}{\alpha_1}h] & \rho_2\exp[\frac{i\omega}{\alpha_2}h] \end{bmatrix} \begin{bmatrix} A_1 \\ B_1 \\ A_2 \end{bmatrix} = \begin{bmatrix} 0 \\ \frac{-i}{\alpha_2}\exp[\frac{-i\omega}{\alpha_2}h]B_2 \\ -\rho_2\exp[\frac{-i\omega}{\alpha_2}h]B_2 \end{bmatrix}$$

The solution for Φ_1 is

$$\Phi_1 = \frac{2\rho_2 \alpha_1 \exp[i\omega h(\frac{1}{\alpha_1} - \frac{1}{\alpha_2})]\{\exp[\frac{i\omega}{\alpha_1}x] - \exp[\frac{-i\omega}{\alpha_1}x]\} B_2}{(\alpha_2 \rho_2 + \alpha_1 \rho_1)\{1 + R\exp[\frac{i\omega}{\alpha_1}2h]\}}$$

where: $R = \dfrac{\rho_2 \alpha_2 - \rho_1 \alpha_1}{\rho_2 \alpha_2 + \rho_1 \alpha_1}$

The velocity at the surface is, therefore,

$$V = i\omega \frac{\partial}{\partial x} \Phi$$

$$= \frac{4\omega^2 \rho_2 \exp[i\omega h(\frac{1}{\alpha_1} - \frac{1}{\alpha_2})] B_2}{(\alpha_2 \rho_2 + \alpha_1 \rho_1)\{1 + R\exp[\frac{i\omega}{\alpha_1}2h]\}}$$

$$= \frac{4\rho_2 \alpha_2 \exp[i\omega h(\frac{1}{\alpha_1} - \frac{1}{\alpha_2})] V_I}{(\alpha_2 \rho_2 + \alpha_1 \rho_1)\{1 + R\exp[\frac{i\omega}{\alpha_1}2h]\}}$$

where: $V_I = \dfrac{\omega^2}{\alpha_2} B_2$

V_I is the Fourier spectrum of the particle velocity of the incident pulse. Expanding

$$\left\{ 1 + R \exp\left[\frac{i\omega}{\alpha_1} 2h\right] \right\}^{-1}$$

in a binomial series gives

$$V = \frac{4\alpha_2\beta_2 \exp\left[i\omega h\left(\frac{1}{\alpha_1} - \frac{1}{\alpha_2}\right)\right]}{(\beta_2\alpha_2 + \beta_1\alpha_1)} \sum_{K=0}^{\infty} (-R)^K \exp\left[\frac{i\omega}{\alpha_1} 2Kh\right] V_I$$

and shows that the resulting surface particle velocity consists of a series of pulses attenuated by $(-R)^K$ and delayed by the times, $2Kh/\alpha_1$.

The modulus of the incident pulse is related to the modulus of the surface pulse by

$$|V| = \frac{4\alpha_2\beta_2 |V_I|}{(\beta_2\alpha_2 + \beta_1\alpha_1)\left\{ R^2 + 1 + 2R\cos\left[\frac{2\omega}{\alpha_1} h\right] \right\}^{1/2}} \cdot$$

APPENDIX II

GNOME traveltime analysis and crustal structure

Figure II-1 maps the locations of the stations along the GNOME refraction line used in this analysis. The station locations are designated by the open squares next to their recording unit code names. The first arrivals at stations India, Hotel, and Kilo have been interpreted as direct arrivals as opposed to head wave arrivals. This identification was based on a comparison of the particle velocities of the first arrivals to the observed source particle velocity (Laun, 1965). Since the other first arrivals appeared similar in waveform, all first arrivals were interpreted as direct arrivals. Also, only correctable lateral variations in structure were assumed to exist. Consequently, curved raypath theory was used to derive the structure directly from the observed data.

The Precambrian surface profile, which can be seen in Figure II-2, was taken along the dashed line extending from the GNOME shot point to the New Mexico-Oklahoma border (Foster and Stipp, 1961). Figure II-2 also shows the corrected first arrival times. The
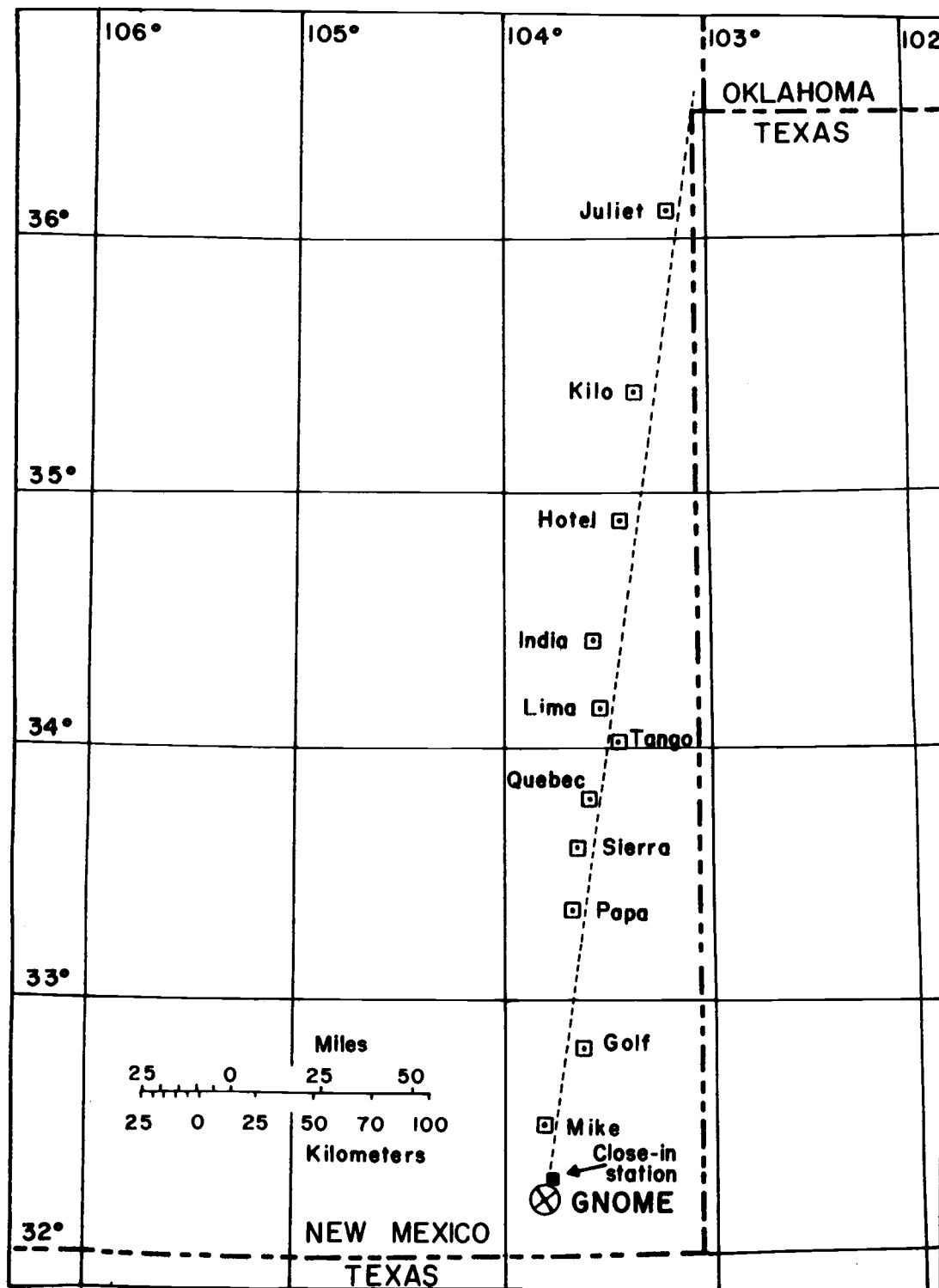
Figure II-1   Locations of GNOME recording stations (after
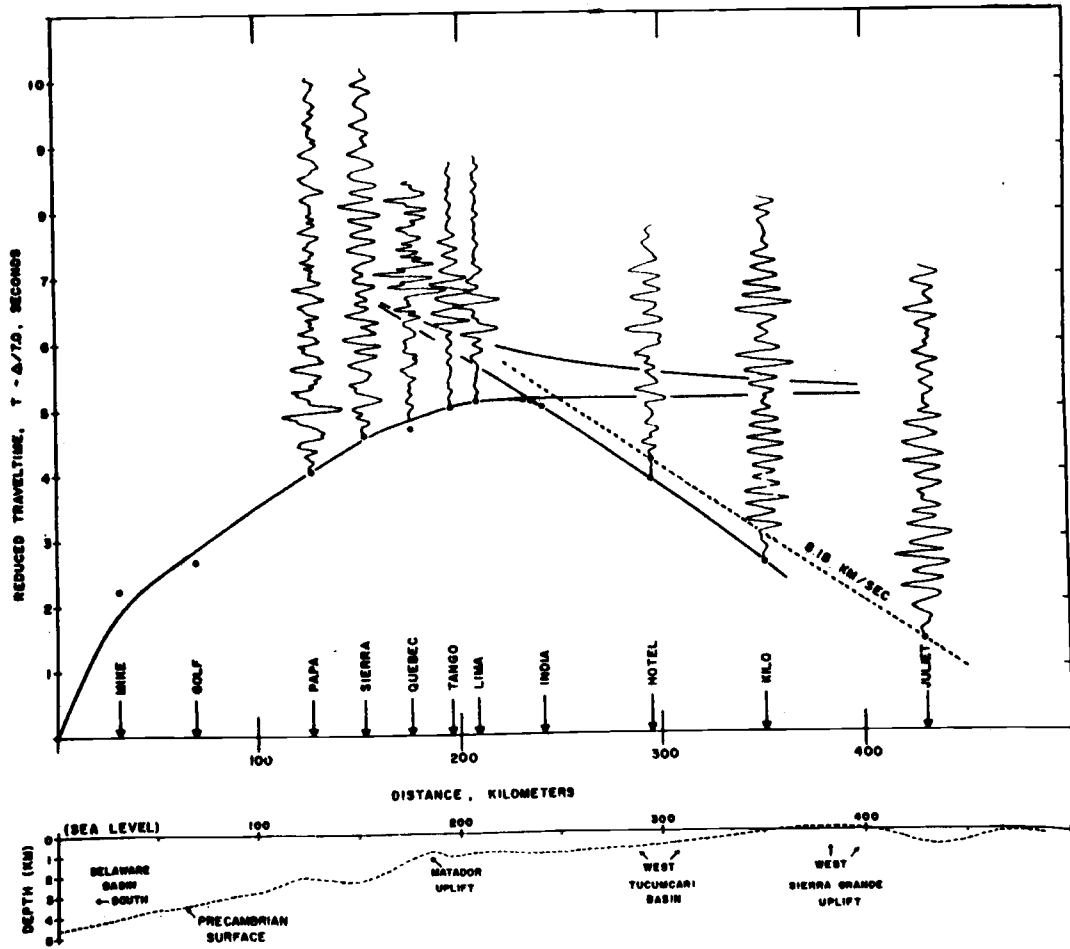Stewart and Pakiser, 1962).

Figure II-2. GNOME reduced traveltime curve, seismic traces and Precambrian structural profile.

arrival times were corrected to a constant elevation datum. In addition, they were corrected for the relief of the Precambrian surface or basement rock. A profile of this surface along the refraction line is shown in the lower portion of Figure II-2. In correcting for the relief of the Precambrian surface, a delay time was calculated for each station by using an average velocity of 4.5 km/sec for the upper layer and a thickness given by the elevation difference between the Precambrian surface beneath the station and the Precambrian surface beneath the GNOME shotpoint. The velocity of 4.5 km/sec was taken from the interpreted traveltime curve which was applicable near the GNOME shotpoint. A closer examination of the corrected traveltimes indicated that a lower velocity would yield a smoother traveltime curve, particularly in the vicinity of station Quebec. The traveltime curve, however, would not be significantly altered. With the possible exceptions of stations Hotel and Juliet, the first arrival times were measurable to within $\pm$ 0.01 sec. However, variations in the velocities of the material above the Precambrian surface could lead to relative uncertainties as large as 0.15 sec.

The traces shown in Figure II-2 were considered typical of the traces recorded at each station. At least one triplication of the traveltime curve was evident in the secondary arrivals. Because of the direct arrival interpretation, a continuous traveltime curve was drawn which included the triplication. The interpreted continuous traveltime curve is shown as a solid line in Figure II-2. Not all the apparent secondary arrivals in Figure II-2 are real since the signal from the GNOME explosion at distance appeared to consist of a primary pulse followed, after a 0.7 sec delay, by a second pulse of equal energy. The two pulses were particularly evident at stations Juliet and Lima. The first arrival at station Hotel was not evident at the amplification shown. The noise level at station Juliet prevented any identification of an earlier arrival, if one exists there. At station India the recording system was overdriven by the signal, and thus only the first arrival could be used.

To calculate a depth versus velocity function, the Weichert-Herglotz-Bateman equation was applied to the interpreted traveltime curve. Figure II-3 shows the velocity profile obtained by including the triplication. The depth versus velocity structure appeared to be
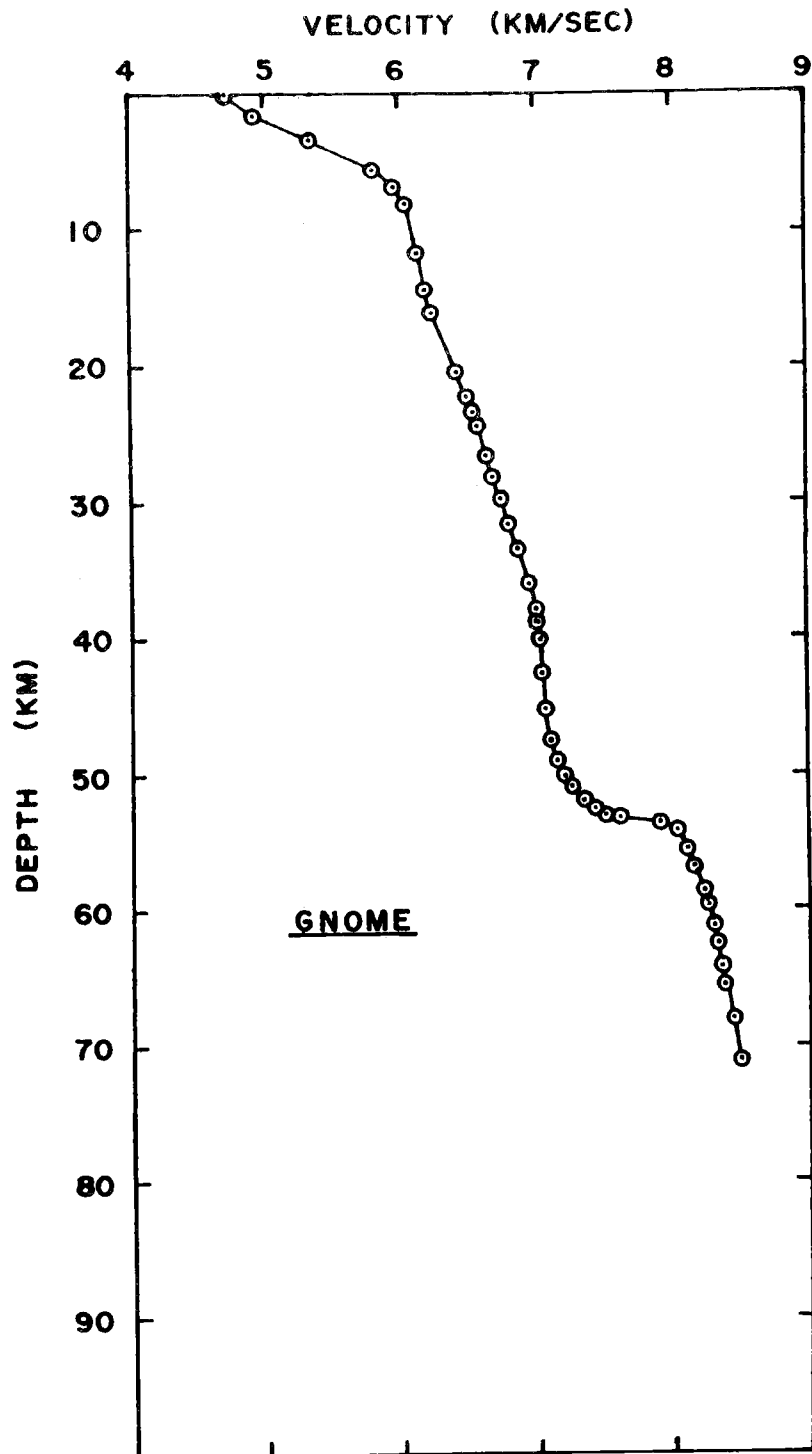
Figure II-3   GNOME velocity versus depth profile.

affected only slightly by variations in the interpreted traveltime curve. The velocity profile included a jump at about 54 km in depth from 7.2 to 8.15 km/sec. The velocity below the jump increased slightly to about 8.35 km/sec. The maximum depth of penetration was 65 km which was determined by the farthest arrival considered in the analysis. A constant or decreasing velocity below this depth could account for the absence or low amplitude of the direct arrival at station Juliet at a range of 430 km.

The depth versus velocity curve was then used to calculate the theoretical amplitude versus distance profile which is shown in Figure II-4. For clarity, two different symbols were used to designate the portions of the interpreted traveltime curve before the crossover point (circles) and after the crossover point (triangles). The observed mean peak-to-trough amplitudes of the first cycle, their standard deviations, and the number of traces used are also shown in Figure II-4. Stewart and Pakiser (1962) indicated that these may be uncertain by as much as $\pm$ 50 percent. The uncertainty for the arrival at 300 km was undoubtedly greater than this because of its low apparent amplitude. Also, focusing of the energy by curvature in the Precambrian surface could affect the amplitudes. At
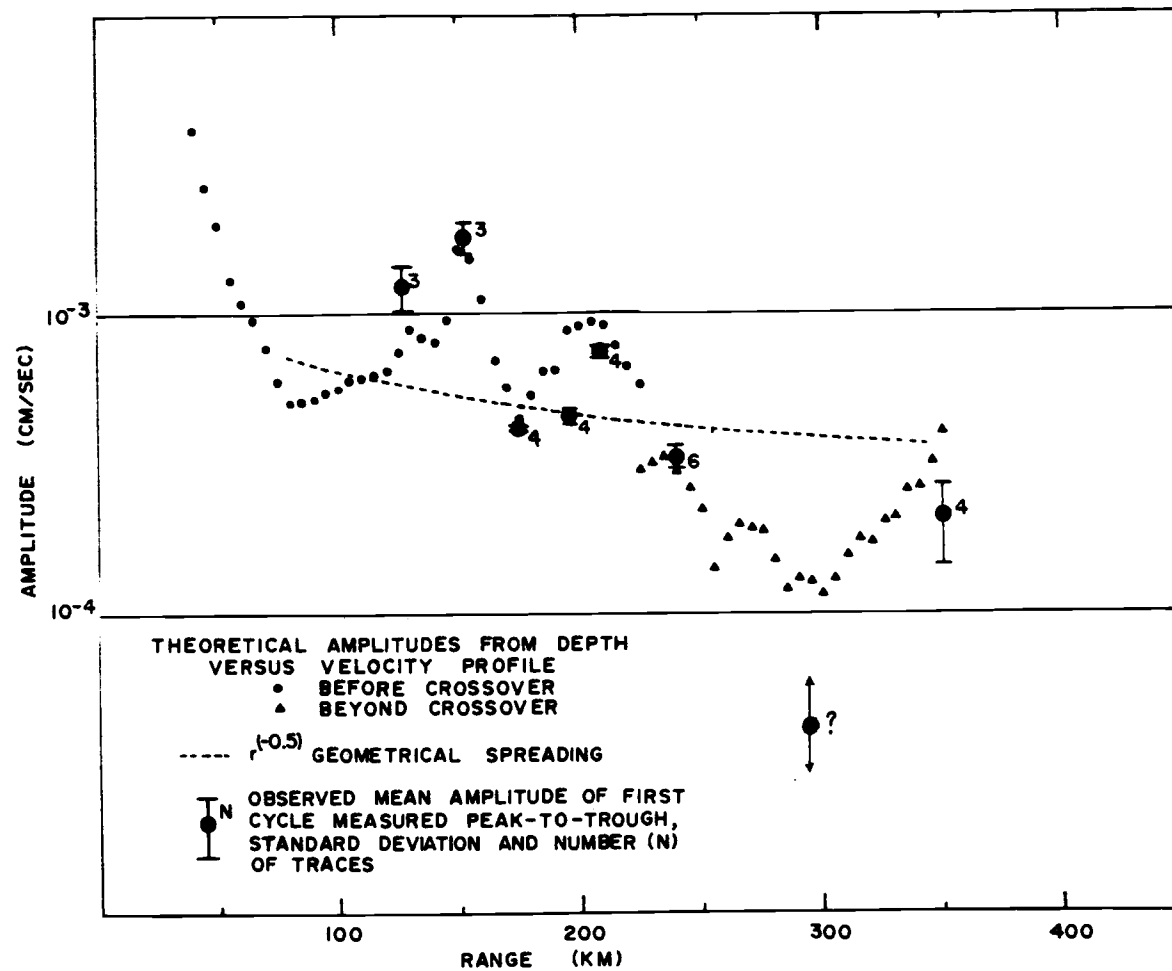
Figure II-4. GNOME amplitude versus distance profile.

a range of about 175 km, this focusing effect appears to correlate with the observed amplitude variations. The theoretical amplitude versus distance profile was calculated from

$$A^2 = P \, Tan(\theta_o) \; / \; (X \frac{\partial X}{\partial \theta_o}) \qquad \text{(Officer, 1958, p.50)}$$

where: P = scale factor;

θ_o = angle of emergence; and

X = horizontal range.

When expressed in apparent velocities, this relation is essentially a second derivative of the interpreted travel-time curve and could be uncertain by a factor of two.

APPENDIX III

SHOAL traveltime analysis and crustal structure

Significant lateral variations in structure along the SHOAL line necessitated an indirect type of analysis in which models were generated until one was found that satisfied the observed data. Consequently, the final crustal structure is undoubtedly only one of many possible modifications that could be made from the crustal models presented by Eaton (1963) and Pakiser (1965).

The locations of the recording units, their code names, and the SHOAL shotpoint are plotted in Figure III-1. A regionalized Bouguer anomaly map together with the regionalized topography (Mabey, 1960) is shown in Figure III-1 also.

The observed reduced traveltimes are plotted in Figure III-2. No time corrections have been applied for variations in elevation or local velocity anomalies. Important secondary arrivals are shown in Figure III-2 also. The theoretical traveltime curve in Figure III-2 corresponds to the crustal model illustrated in Figures III-3a and III-3b. The regionalized Bouguer gravity profile along the refraction line is shown in Figure III-3c.
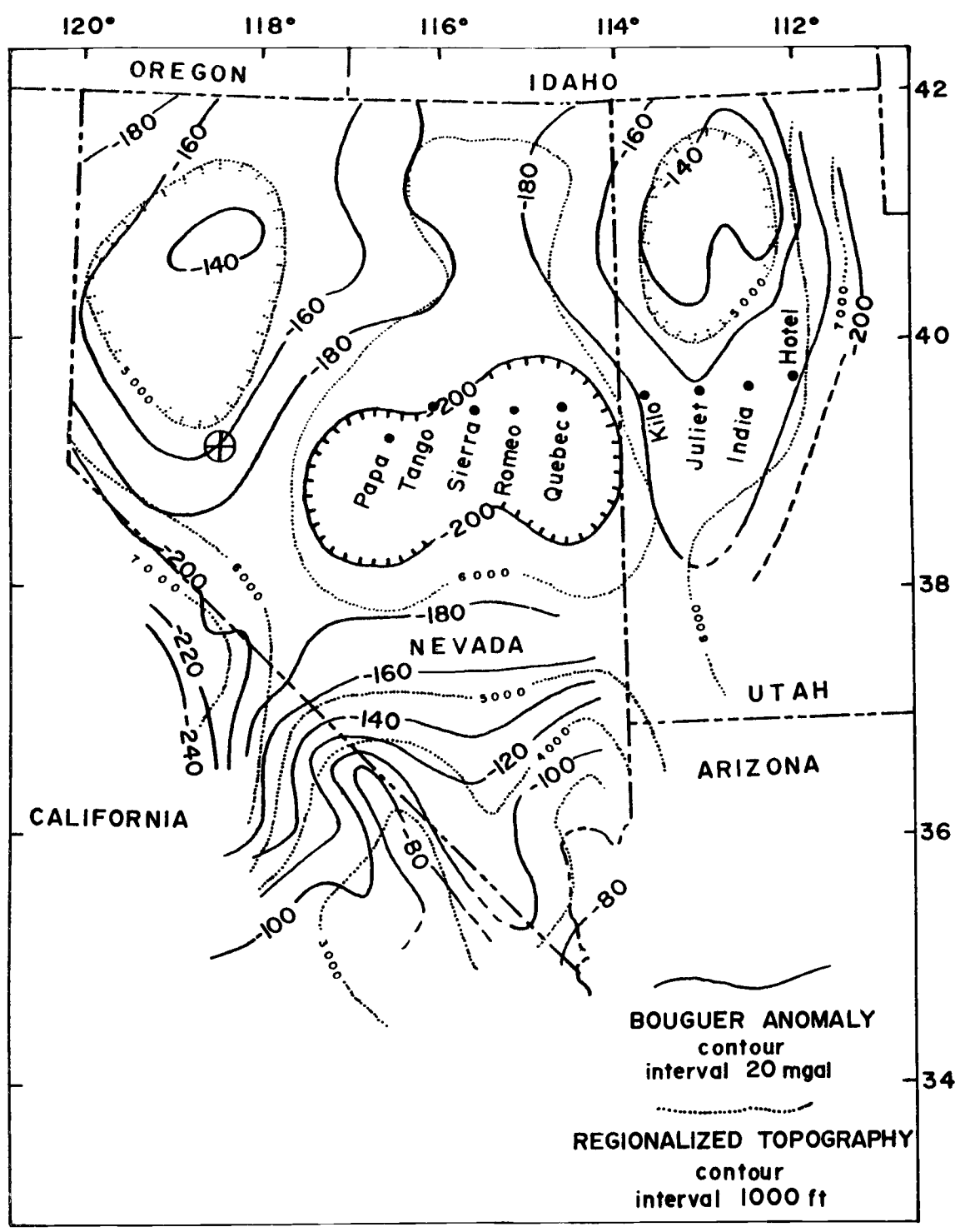
Figure III-1   Map showing locations of SHOAL shotpoint
and recording sites, regionalized eleva-
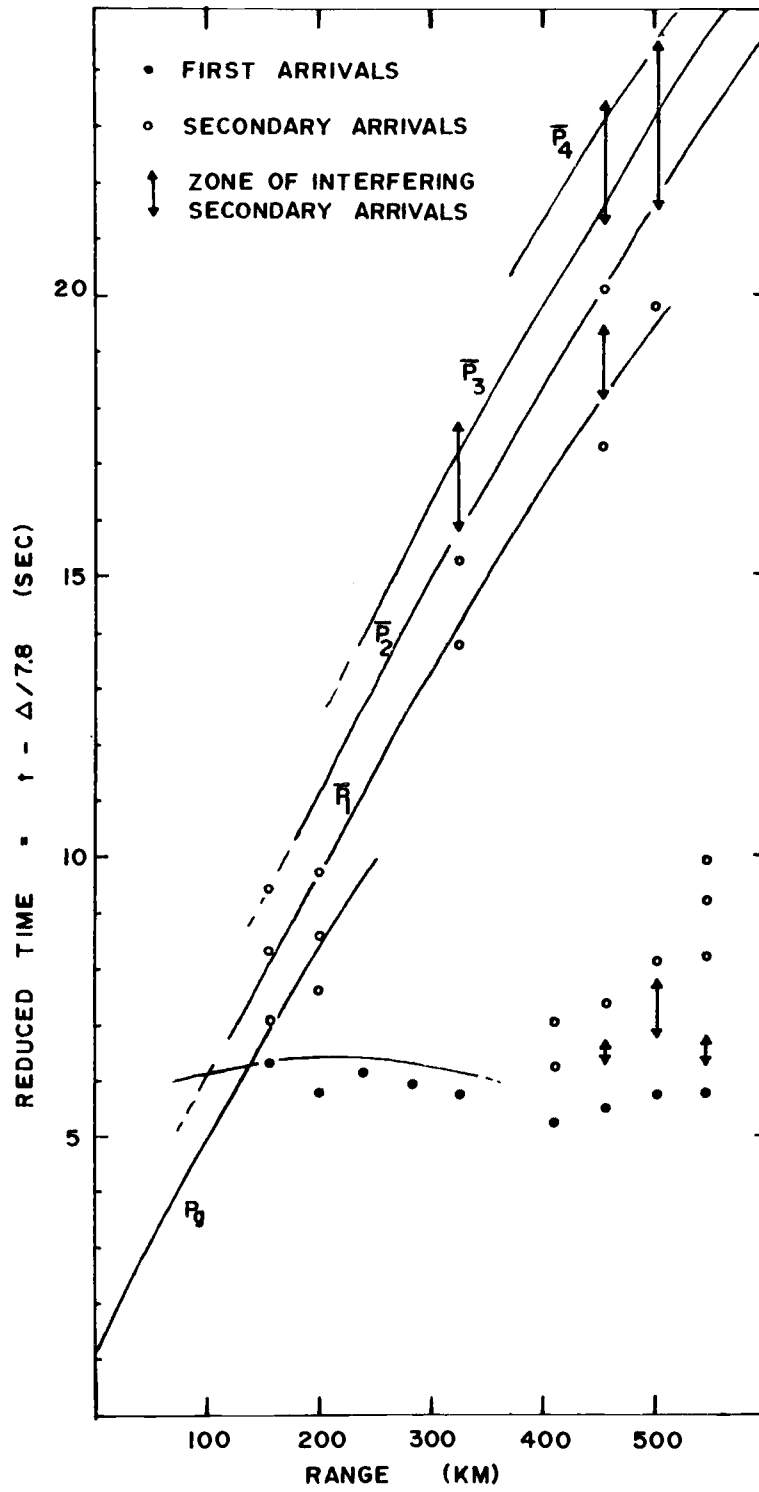tion and regionalized Bouguer anomaly
(after Mabey, 1960).

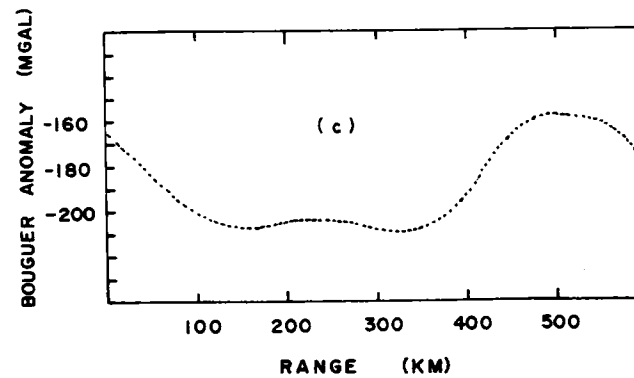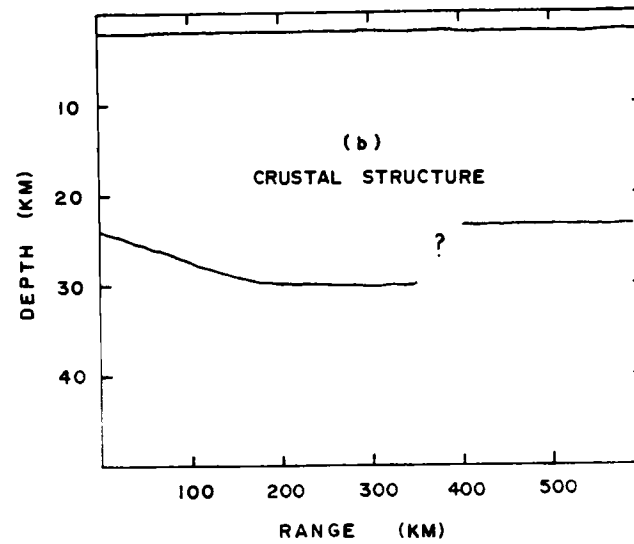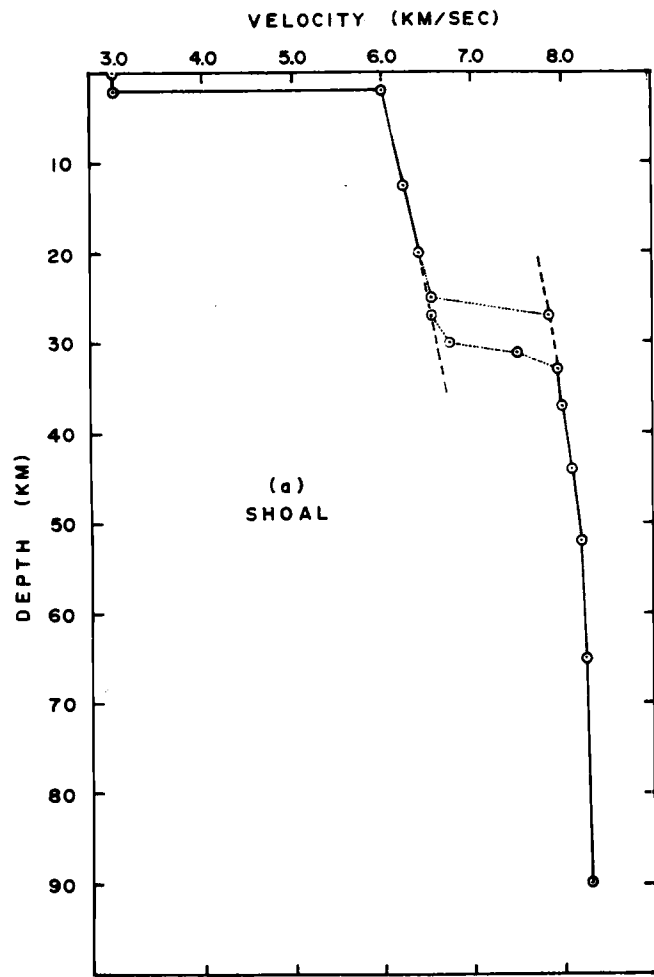Figure III-2   SHOAL reduced traveltime curve.

Figure III-3. SHOAL profiles: (a) velocity versus depth profile, (b) crustal cross section, (c) Bouguer anomaly.

Amplitude measurements are shown in Figure III-4. The
error limits shown represent one standard deviation of
the measurable traces at each station. Stations Romeo,
Quebec, Kilo and Juliet showed an amplitude decrease with
distance, and station India showed an increase with dis-
tance. The number of traces used in stacking is indicated
next to each station where limits of variation are given.
A high-frequency (nine cps) rider on station India may
have caused this measure to be anomalously high.

The following analysis refers to the velocity versus
depth function and curstal structure in Figures III-3a
and III-3b. A velocity of three km/sec and a thickness
of two km was chosen to represent the average effect of
the surface layers. The thickness and velocity were sug-
gested by the intercept times observed by Eaton (1963) for
the P_g arrival. Secondary arrivals, $\overline{P}$ and P_g, of the
SHOAL event shown in Figure III-2 also suggest an effect
of this magnitude.

The lack, in the SHOAL data, of secondary arrivals
of significant energy to indicate a distinct intermediate
layer prompted the use of a velocity gradient in the crust.
The velocity of 6.6 km/sec at the base of the crust cor-
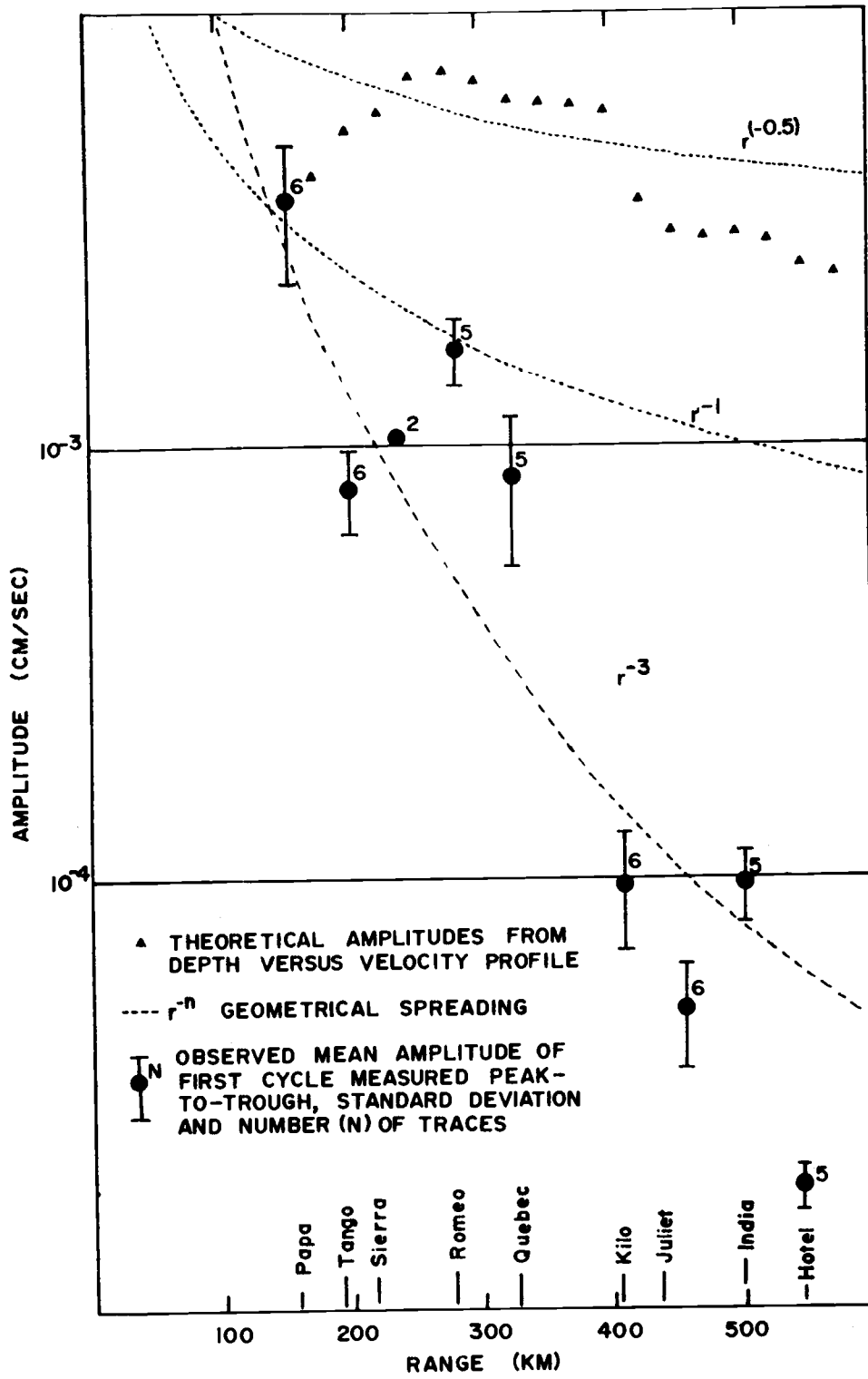responds to a velocity suggested by Eaton (1963) for an

Figure III-4   SHOAL amplitude versus distance profile.

intermediate layer he considered questionable. The slope

of 30 M/km in the Moho in the western portion was inter-

preted from the data given by Eaton (1963) for a reversed

refraction line between Fallon and Eureka, Nevada, and

variations in the regional Bouguer gravity anomalies

support this interpretation. Below the Moho the velocity

gradient is positive down to a depth of about 60 km where

it attains the velocity of 8.2 km/sec and becomes constant

or decreases. The observed amplitudes show a focusing of

energy from 200 to 350 km which could partially be due to

slight variations in the gradient below the Moho. The

theoretical amplitudes in Figure III-4 calculated from the

depth versus velocity profile also predict a focusing of

energy from 200 to 350 km.

A marked change, exhibited by all the data along the

SHOAL refraction line, occurs between 325 and 400 km and

is designated in the crustal model, Figure III-3b, by a

zone of questionable structure. The average elevation

drops from 6000 ft to 5000 ft. The regionalized Bouguer

anomaly increases from -210 to -160 mgal, indicating a

decrease in the depth to the Moho or an excess of high

density material. The time differences on the traveltime

curve for the earlier arrivals beyond 350 km also indicate

a shallower depth of 23 km to the Moho. The observed apparent velocity of 7.6 km/sec is close to the velocity obtained by extending the lower velocity gradient up to 23 km. Beyond 350 km the amplitude is attenuated by a factor of ten also reflecting a change in crustal structure. Other refraction studies in the region characterized by the high Bouguer gravity anomaly (Berg et al., 1960) indicate a Moho velocity of about 7.6 km/sec at a depth of 25 km. The interpreted change in crustal structure undoubtedly includes the upper mantle but no evidence concerning lower layers or velocity structure was identified in the SHOAL data.

The positive velocity gradient below the free surface and the Moho creates two energy channels in which continuously refracted seismic waves are repeatedly reflected downward on striking the boundaries. The $\bar{P}$ arrivals for SHOAL show evidence for channeling in the crust and the immediate secondary arrivals beyond 300 km show evidence for channeling below the Moho.

The theoretical traveltime curves for up to four reflections of continuous refraction in the crustal channel, Figure III-2, compare well with the observed distribution of arrivals. The observed delay times of

about 1.2 sec compare favorably to the expected delay time

for the low-velocity surface layers. $\overline{P}_1$ (P_g) and $\overline{P}_2$ end at

about 250 and 500 km respectively, because at these ranges

they are just grazing the Moho. Higher order reflections

off the free surface probably are not seen at closer ranges

because of the irregularities in structure near the surface

and conversion at the surface to other types of waves.

Consequently, the effective group velocity of the $\overline{P}$

arrivals ranges from 5.7 to 6.2 km/sec, Figure III-2. The

higher 6.6 km/sec velocity is not seen because of the time

delay on reflection from the free surface caused by the

low-velocity surface layers. The $\overline{P}$ arrivals generally

consist of lower frequencies (Ryall and Stuart, 1963).

The lower frequency character may be attributed to a com-

bination of effects related to: greater attenuation in

the surface layers, scattering from structural irregula-

rities, and the number of times the arrival has been re-

turned to the surface.

The energy channel created by the Moho and the posi-

tive velocity gradient below offers an explanation for

the complexity of the P_n arrival and its immediate

secondary arrivals. The amplitudes of the arrivals ob-

served at the surface, however, depend strongly on the

reflection and refraction coefficients which in turn depend on the angle of incidence and the velocity contrasts at the Moho. Consequently, slight variations in the velocity, dip, or smoothness of the Moho could strongly affect the observed amplitudes. Variations in the gradient below the Moho could also cause a variation in the amplitudes by focusing the rays. In particular, the constant or decreasing velocity below 60 km depth would attenuate the direct arrival at greater ranges and cause the reflected refraction to appear larger. There is only a very slight or no time delay upon reflection since there is only a weak positive velocity gradient beneath the Moho. A time delay does arise, however, from the travelpaths through the crust associated with the different angles of emergence. For the SHOAL velocity structure at 304 km, the time difference between the direct arrival and one which has been reflected once off the bottom of the Moho is 0.34 sec. The immediate secondary arrivals along the SHOAL line from 400 to 550 km would be reflected refractions of the large amplitude first arrivals observed from 250 to 325 km.